



UNIVERSITY OF LEEDS

This is a repository copy of *Penetration of boundary-driven flows into a rotating spherical thermally stratified fluid*.

White Rose Research Online URL for this paper:
<http://eprints.whiterose.ac.uk/142544/>

Version: Accepted Version

Article:

Cox, GA, Davies, CJ orcid.org/0000-0002-1074-3815, Livermore, PW
orcid.org/0000-0001-7591-6716 et al. (1 more author) (2019) Penetration of boundary-driven flows into a rotating spherical thermally stratified fluid. *Journal of Fluid Mechanics*, 864. pp. 519-553. ISSN 0022-1120

<https://doi.org/10.1017/jfm.2018.999>

Reuse

Items deposited in White Rose Research Online are protected by copyright, with all rights reserved unless indicated otherwise. They may be downloaded and/or printed for private study, or other acts as permitted by national copyright laws. The publisher or other rights holders may allow further reproduction and re-use of the full text version. This is indicated by the licence information on the White Rose Research Online record for the item.

Takedown

If you consider content in White Rose Research Online to be in breach of UK law, please notify us by emailing eprints@whiterose.ac.uk including the URL of the record and the reason for the withdrawal request.



eprints@whiterose.ac.uk
<https://eprints.whiterose.ac.uk/>

Penetration of boundary-driven flows into a rotating spherical thermally-stratified fluid

Grace A. Cox^{1,2,*†}, Christopher J. Davies³, Philip W. Livermore³,
and James Singleton³

¹School of Environmental Sciences, University of Liverpool, Liverpool, L69 3GP, UK

²Department of Applied Mathematics, University of Leeds, Leeds, LS2 9JT, UK

³School of Earth and Environment, University of Leeds, Leeds, LS2 9JT, UK

*Now at the Dublin Institute for Advanced Studies, Geophysics section, Dublin, Ireland

(Received xx; revised xx; accepted xx)

1 Motivated by the dynamics within terrestrial bodies, we consider a rotating, strongly
2 thermally stratified fluid within a spherical shell subject to a prescribed laterally inhomogeneous
3 heat-flux condition at the outer boundary. Using a numerical model, we explore
4 a broad range of three key dimensionless numbers: a thermal stratification parameter
5 (the relative size of boundary temperature gradients to imposed vertical temperature
6 gradients), $10^{-3} \leq S \leq 10^4$, a buoyancy parameter (the strength of applied boundary
7 heat flux anomalies), $10^{-2} \leq B \leq 10^6$, and the Ekman number (ratio of viscous to
8 Coriolis forces), $10^{-6} \leq E \leq 10^{-4}$. We find both steady and time-dependent solutions
9 and delineate the temporal regime boundaries. We focus on steady-state solutions, for
10 which a clear transition is found between a low S regime, in which buoyancy dominates
11 dynamics, and a high S regime, in which stratification dominates. For the low- S regime,
12 we find that the characteristic flow speed scales as $B^{2/3}$, whereas for high- S , the radial
13 and horizontal velocities scale respectively as $u_r \sim S^{-1}$, $u_h \sim S^{-3/4} B^{1/4}$ and are confined
14 to boundary-induced flow within a thin layer of depth $(S B)^{-1/4}$ at the outer edge of

† Email address for correspondence: gracecox@cp.dias.ie

15 the domain. For the Earth, if lower-mantle heterogeneous structure is due principally to
16 chemical anomalies, we estimate that the core is in the high- S regime and steady flows
17 arising from strong outer-boundary thermal anomalies cannot penetrate the stable layer.
18 However, if the mantle heterogeneities are due to thermal anomalies and the heat-flux
19 variation is large, the core will be in a low- S regime in which the stable layer is likely
20 penetrated by boundary-driven flows.

21 **1. Introduction**

22 Differential heating at the boundary of a stratified fluid arises in a variety of physical
23 systems. The oceans and atmosphere are heated non-uniformly from above owing to the
24 latitudinal variation of incoming solar energy. Fluid near the differentially heated surface
25 moves laterally away from anomalously warm regions towards anomalously cold regions
26 and a significant amount of work has considered whether this ‘horizontal convection’
27 can drive large-scale overturning circulations (e.g. Paparella & Young 2002; Siggers *et al.*
28 2004; Sheard *et al.* 2016; Shishkina 2017). The primary motivation for the present study is
29 differential heating of planetary cores due to lateral heat flow anomalies in their overlying
30 solid mantles. We conduct a systematic investigation of the interaction between thermal
31 stratification and differential boundary heating, incorporating the key ingredients of
32 rapid rotation and spherical shell geometry. Our main focus is to establish the extent to
33 which boundary heat flow anomalies can penetrate and disrupt a pre-existing thermal
34 stratification.

35 There is now a body of evidence indicating that the cores of Mercury (Christensen
36 2006), Earth (Davies *et al.* 2015; Nimmo 2015), Mars (Stevenson 2001) and Ganymede
37 (Rückriemen *et al.* 2015) are thermally stably stratified below the core-mantle boundary
38 (CMB) owing to a subadiabatic CMB heat flow, with convection (and magnetic field

39 generation) arising at greater depths. The existence of stratification is important because
40 it influences the intensity and structure of the observable magnetic field (Christensen
41 2006; Stanley & Glatzmaier 2010) and reflects the core's long-term evolution. The
42 strength and thickness of these thermally stable regions is hard to assess due to a
43 lack of direct observations. The stable layer in Earth's core could be up to ~ 700 km
44 thick (Gubbins *et al.* 2015) with a Brunt-Väisälä frequency comparable to the rotation
45 period. Thermal stratification in the Martian core is usually estimated to have begun
46 around 4 Ga, corresponding to the epoch when the planet lost its global magnetic field
47 (Stevenson 2001), and so the thermally stable region could occupy a significant fraction
48 of the present-day core. Thermal history models for Ganymede predict a stable layer
49 hundreds of kilometres thick (Rückriemen *et al.* 2015).

50 Terrestrial planetary cores are overlain by rocky mantle, which acts like a viscous
51 fluid convecting on timescales of 10^8 years. In contrast, liquid metal cores have very low
52 viscosity and convect on timescales of 10^3 years. This difference in convection timescales
53 means that the core responds to the CMB as a rigid surface with a fixed heat flux
54 imposed by the lower mantle, whilst the mantle is subjected to a uniform temperature
55 lower boundary condition (Olson & Christensen 2002). Mantle convection simulations
56 produce lateral temperature anomalies of thousands of Kelvin and lateral CMB heat
57 flow variations greater than the mean CMB heat flow (e.g. Nakagawa & Tackley 2008;
58 Olson *et al.* 2015). These lateral variations will inevitably drive baroclinic flows in the
59 underlying core through the thermal wind, but it is unclear the extent to which they will
60 drive penetrative flow within a strongly stratified region.

61 The competition between stratification and boundary forcing has been explored in
62 some numerical studies of convection in nonmagnetic rotating spherical shells, which
63 have shown that thermal boundary anomalies are capable of drastically altering the

64 dynamics compared to uniform thermal boundary conditions (e.g. Zhang & Gubbins
65 1992, 1993; Gibbons & Gubbins 2000; Gibbons *et al.* 2007). Zhang & Gubbins (1992)
66 solved for steady flows driven by lateral thermal variations at the outer boundary of a
67 rotating spherical shell, having specified temperature rather than heat flux for numerical
68 simplicity. They studied both unstratified and weakly stratified fluids subjected to a
69 range of temperature anomaly patterns and magnitudes. For modest boundary anomaly
70 strengths, patterns of temperature fluctuations and fluid flow lock to the boundary
71 anomaly pattern through the thermal wind, and flows penetrate deep into the shell
72 due to Coriolis effects. Stratification greatly reduces radial flow amplitudes, though
73 toroidal flows are less affected, and confine flow towards the outer boundary. The authors
74 speculated that these results would also be obtained in the geophysical case of fixed
75 heat flux boundary anomalies. Gibbons & Gubbins (2000) were able to confirm this
76 for steady flows in their subsequent investigation of weakly stratified fluids in rotating
77 spherical shells. They applied different spatial distributions and magnitudes of large-
78 scale boundary heat flow anomalies to fluids of varying stratification strengths. For
79 equatorially symmetric patterns, rotational effects dominate dynamics at weak or no
80 stratification. As the stratification increases, rotational effects become less important,
81 radial flow diminishes and flow is confined to a layer beneath the outer boundary.
82 Smaller length scale heat flux patterns drive less energetic flows that are not able to
83 penetrate as deeply into the fluid. Solutions become increasingly smaller scale with
84 increasing boundary anomaly magnitude, with correspondingly higher computational
85 expense. Gibbons & Gubbins (2000) suggested that solutions would become unstable
86 (time-dependent) with sufficiently strong boundary anomalies, though computational
87 limitations prevented the authors from identifying the parameters at which this occurs.
88 Several authors have considered the more realistic but more complex magnetohy-

89 hydrodynamic (MHD) case by studying numerical simulations of dynamos in partially
90 stratified spherical shells, including Christensen (2006); Christensen & Wicht (2008);
91 Stanley & Mohammadi (2008); Aurnou & Aubert (2011); Nakagawa (2011, 2015); Olson
92 *et al.* (2017). Some numerical models have shown that the presence of a stable layer
93 fundamentally changes dynamo action and can drastically alter the magnetic field at the
94 planetary surface compared to equivalent models with no stable layer. For example,
95 Christensen (2006) showed that a strong magnetic field at the top of the dynamo
96 generating region diffuses through a stable layer such that the small-scale, rapidly varying
97 components are filtered out.

98 Dynamo models with heterogeneous thermal boundary conditions have also been
99 investigated by various authors, see the review by Amit *et al.* (2015) and references
100 therein. As in the non-magnetic case, within MHD models heterogeneous boundary
101 forcing has been shown to have a significant effect, for example by modifying the
102 morphology of the magnetic field (e.g. Olson & Christensen 2002; Gubbins *et al.* 2007;
103 Aurnou & Aubert 2011) such that its long-term fundamental symmetries follow the
104 spatial symmetries of the imposed heat flux pattern, or by locking the magnetic field
105 to regions of anomalously high heat flow (Willis *et al.* 2007; Sreenivasan 2009). In some
106 circumstances, strong boundary driven flows can also overwhelm the convection such
107 that dynamo action is weakened or destroyed altogether (Olson & Christensen 2002;
108 Takahashi *et al.* 2008), though this is not necessarily the case (Aurnou & Aubert 2011).
109 Although ultimately the most physically relevant model, a thorough scaling analysis of
110 the competition between stratification and boundary forcing within an MHD setting is
111 beyond what is currently achievable. Some progress has been made by studying weakly
112 stratified models with heterogeneous outer boundary conditions (e.g. Sreenivasan &

113 Gubbins 2008; Aurnou & Aubert 2011; Olson *et al.* 2017), although the extrapolation
114 gap from the parameters used in these models to realistic values is large.

115 This work focusses on the simpler, non-magnetic problem which is yet not fully
116 described. In particular, the previous studies described above have been limited to highly
117 viscous, weakly-stratified fluids in spherical shells with moderate rotation rates and
118 subject to relatively weak boundary anomalies: it is not clear how these results bear on the
119 rapidly rotating, strongly stratified case relevant to planetary cores that are additionally
120 subject to significant lateral variations in heat flux at their outer boundary. One severe
121 computational limitation that has hampered progress arises because rotating flows adopt
122 small azimuthal length scales even at the onset of convection (Chandrasekhar 1961), while
123 increasing the amplitude of the driving force generates a broad spectrum of flow structures
124 that become increasingly difficult to resolve. In this study, we minimise this problem
125 by considering a subset of steady-state solutions obtained from solving the full time-
126 dependent equations, and also by assuming that the entire fluid domain is stably stratified
127 without any internal heat sources that drive internal convection. This is equivalent to
128 assuming that any underlying convection does not significantly penetrate or mix an
129 overlying stable region, which is true in the case of strong stratification (Takehiro &
130 Lister 2001; Buffett & Seagle 2010; Gubbins & Davies 2013). These assumptions allow us
131 to isolate the interaction between outer-boundary forcing and pre-existing stratification,
132 without the additional complication of destabilisation of stratified fluid from below by
133 internal convection, and to study the dynamics using a much wider range of parameters
134 than has been possible previously.

135 The fluid dynamical problem we consider depends upon three dimensionless numbers
136 (detailed definitions are given in 2.1): a thermal stratification parameter, S , defined
137 as the relative size of boundary temperature gradients to imposed vertical temperature

138 gradients, a buoyancy parameter, B , measuring the strength of the applied boundary heat
139 flux anomalies, and the Ekman number, E , the ratio of viscous and Coriolis forces. Our
140 study spans the ranges $10^{-2} \leq B \leq 10^6$, $10^{-3} \leq S \leq 10^4$ and $10^{-6} \leq E \leq 10^{-4}$. We focus
141 primarily on the case where the aspect ratio, the ratio of inner to outer boundary radii,
142 corresponds to that of Earth's liquid core, $r_i/r_o = \eta = 0.35$. Additional simulations are
143 performed at $\eta = 0.01$, which is almost a full sphere and approximates the core geometry
144 of Mars and Ganymede.

145 For each choice of (E, S, B) a heat flow pattern must be chosen. Previous studies clearly
146 show that the influence of thermal boundary anomalies on the structure and dynamics
147 of rotating fluids becomes more pronounced as the lengthscale of the imposed pattern
148 is increased (Zhang & Gubbins 1992, 1993; Davies *et al.* 2009). We choose to apply
149 a Y_2^2 spherical harmonic boundary heat flow pattern since this the largest component
150 of shear wave variation (a likely proxy for CMB heat flow) in Earth's lower mantle
151 (Dziewonski *et al.* 2010); it is also a common boundary condition of previous studies,
152 which makes comparison straightforward (e.g. Zhang & Gubbins 1992, 1993; Davies *et al.*
153 2009; Sreenivasan 2009; Sahoo & Sreenivasan 2017).

154 We have conducted a suite of 99 numerical simulations finding predominantly steady
155 solutions, which partition into two distinct regimes. Within each regime we formulate
156 theoretical scaling laws that provide excellent fits to our dataset and permit extrapolation
157 to the parameter regimes appropriate to planetary interiors. The remainder of the paper is
158 structured as follows: the mathematical formulation is given in §2, results of the numerical
159 simulations are presented in §3, scaling analyses and their application to Earth and
160 Ganymede's outer cores follow in §4 and §5, and a summary of results is found in §6.

161 2. Method

162 We consider an incompressible Boussinesq fluid in an impenetrable spherical shell, of
 163 outer radius r_o and inner radius r_i , rotating about the axial $\hat{\mathbf{z}}$ direction with constant
 164 angular velocity Ω . The whole shell is thermally stratified and compositional effects are
 165 neglected, as in Gibbons & Gubbins (2000), in order to isolate the effects of thermal
 166 boundary anomalies on a thermally stratified fluid. Again following Gibbons & Gubbins
 167 (2000), we also neglect the magnetic field so as to reach more realistic E , B and S
 168 values; the effects of free convection and the resulting magnetic field evolution will be
 169 investigated in a future study. In the following work, r , θ and ϕ denote spherical polar
 170 coordinates, \mathbf{r} is the position vector and t is time.

171 2.1. Governing equations and non-dimensionalisation

172 Following the formulation of Zhang & Gubbins (1992) and Gibbons & Gubbins (2000),
 173 the temperature is split into a steady radial part, T_0 , and a time-varying part, T_1 , such
 174 that

$$T(r, \theta, \phi, t) = T_0(r) + T_1(r, \theta, \phi, t). \quad (2.1)$$

175 The steady radial temperature profile satisfies

$$\kappa \nabla^2 T_0 = F, \quad (2.2)$$

176 where κ is the thermal diffusivity and $F \geq 0$ is a heat sink, and is chosen to impose a
 177 background thermal gradient that, if strong, suppresses radial motion. Integrating with
 178 respect to r in spherical coordinates gives

$$r^2 \frac{dT_0}{dr} = \beta r^3 + A \quad (2.3)$$

179 where $\beta = \frac{F}{3\kappa}$ and A is a constant of integration. Setting the outer boundary condition
 180 such that

$$\left. \frac{dT_0}{dr} \right|_{r=r_o} = \beta r_o \quad (2.4)$$

181 results in $A = 0$ and so within the spherical shell $\frac{dT_0}{dr} = \beta r$.

182 We define the outer boundary condition of the temperature gradient as

$$\left. \frac{\partial T_1}{\partial r} \right|_{r=r_o} = \mathcal{H} Y_2^2(\theta, \phi), \quad (2.5)$$

183 in which the spatial pattern of the anomaly is given by the spherical harmonic $Y_2^2(\theta, \phi)$,
 184 and the magnitude of the anomaly is given by \mathcal{H} . Rewriting the general temperature
 185 equation

$$\frac{\partial T}{\partial t} + (\mathbf{u} \cdot \nabla)T = \kappa \nabla^2 T - F, \quad (2.6)$$

186 using (2.1) and (2.4) leaves

$$\frac{\partial T_1}{\partial t} + (\mathbf{u} \cdot \nabla)T_1 + u_r \beta r = \kappa \nabla^2 T_1 \quad (2.7)$$

187 as the relevant temperature equation.

188 The equations for conservation of momentum in a rotating frame of reference and for
 189 conservation of mass are

$$\frac{\partial \mathbf{u}}{\partial t} + (\mathbf{u} \cdot \nabla)\mathbf{u} + 2\Omega(\hat{\mathbf{z}} \times \mathbf{u}) = -\nabla \left(\frac{P'}{\rho_0} \right) + \frac{\rho' \mathbf{g}}{\rho_0} + \nu \nabla^2 \mathbf{u} \quad (2.8)$$

190 and

$$\nabla \cdot \mathbf{u} = 0 \quad (2.9)$$

191 where \mathbf{u} is velocity, P' is the pressure perturbation, ρ_0 is a reference density, ρ' is
 192 the deviation from the reference density, \mathbf{g} is gravity and ν is the kinematic viscosity.

193 Expressing ρ' as

$$\rho' = -\rho_0 \alpha_T T_1, \quad (2.10)$$

194 where α_T is the coefficient of thermal expansivity, gives an alternative form of the
195 momentum equation

$$\frac{\partial \mathbf{u}}{\partial t} + (\mathbf{u} \cdot \nabla) \mathbf{u} + 2\Omega(\hat{\mathbf{z}} \times \mathbf{u}) = -\nabla \hat{P} + \alpha_T \gamma T_1 \mathbf{r} + \nu \nabla^2 \mathbf{u}, \quad (2.11)$$

196 where \hat{P} is the reduced pressure ($= P'/\rho_0$) and γ is a constant ($\mathbf{g} = -\gamma \mathbf{r}$).

197 Scaling radius by a characteristic length scale d ($= r_o - r_i$), time by the thermal
198 diffusion time d^2/κ , velocity by κ/d and temperature by $\mathcal{H}d$ (from equation (2.5)) gives
199 the radial temperature profile and the temperature and momentum equations in their
200 dimensionless forms

$$\frac{dT_0^*}{dr^*} = S r^*, \quad (2.12)$$

201

$$\frac{\partial T_1^*}{\partial t^*} + (\mathbf{u}^* \cdot \nabla) T_1^* + S u_r^* r^* = \nabla^2 T_1^* \quad (2.13)$$

202 and

$$\frac{E}{Pr} \left[\frac{\partial \mathbf{u}^*}{\partial t^*} + (\mathbf{u}^* \cdot \nabla) \mathbf{u}^* \right] + (\hat{\mathbf{z}}^* \times \mathbf{u}^*) = -\nabla \hat{P} + B T_1^* \mathbf{r}^* + E \nabla^2 \mathbf{u}^*, \quad (2.14)$$

203 where \mathbf{r}^* is the dimensionless radial vector, S is the stratification parameter, E is the
204 Ekman number, Pr is the Prandtl number and B is the buoyancy parameter. These
205 dimensionless numbers are defined as

$$S = \frac{\beta d}{\mathcal{H}}, E = \frac{\nu}{2\Omega d^2}, Pr = \frac{\nu}{\kappa}, B = \frac{\alpha_T \gamma \mathcal{H} d^3}{2\Omega \kappa}, \quad (2.15)$$

206 and B is related to E and a Rayleigh number, $Ra_{\mathcal{H}}$, where

$$\frac{B}{E} = Ra_{\mathcal{H}} = \frac{\alpha_T \gamma \mathcal{H} d^5}{\nu \kappa}. \quad (2.16)$$

207 In this work, all calculations are performed at $Pr = 1$ for numerical convenience and the
 208 majority with a shell aspect ratio $\eta = 0.35$; a summary of model parameters is given in
 209 tables A.1 to A.4 in appendix A. We investigate the effects of varying the shell aspect
 210 ratio using models with $\eta = 0.01$ in section 4.3. The governing equations are solved for
 211 \mathbf{u} and T_1 with no-slip boundary conditions on both inner and outer boundaries, a fixed
 212 temperature of zero imposed on the inner boundary, and a fixed heat flux imposed on
 213 the outer boundary as previously discussed. A detailed description of the pseudo-spectral
 214 code may be found in Willis *et al.* (2007) and Davies *et al.* (2011), and in the most recent
 215 dynamo benchmark paper (Matsui *et al.* 2016). Although equations (2.1) – (2.5) give the
 216 clearest mathematical description of our method, in fact the code solves the following
 217 equation

$$\frac{\partial T^*}{\partial t^*} + (\mathbf{u}^* \cdot \nabla) T^* = \nabla^2 T^* - 3 S, \quad (2.17)$$

218 which is equivalent to (2.13). To benchmark our code for this particular problem, we
 219 reproduced the flow magnitudes and spatial patterns reported in Gibbons & Gubbins
 220 (2000), using a shell aspect ratio $\eta = 0.4$ and their parameters of $E = 10^{-3}$, $Pr = 1$,
 221 $B = 1$ and $S = 0$ and $S = 100$.

222 Given that we focus upon steady-state solutions to the time-dependent equations,
 223 for numerical expediency where possible we used the final steady-state solution of a
 224 model nearby in parameter space as the initial condition. Models were run long past
 225 the initial transient period and until the volume-averaged kinetic energy converged to
 226 a steady value. Several numerical models were unstable and no steady-state solutions
 227 were obtained at those parameters. In such cases, we cannot rule out the existence of a
 228 steady-state model using different initial conditions.

229 For each of our models, spatial convergence was verified by assessing the kinetic
 230 energy power spectrum as a function of spherical harmonic degree (l) and order (m).

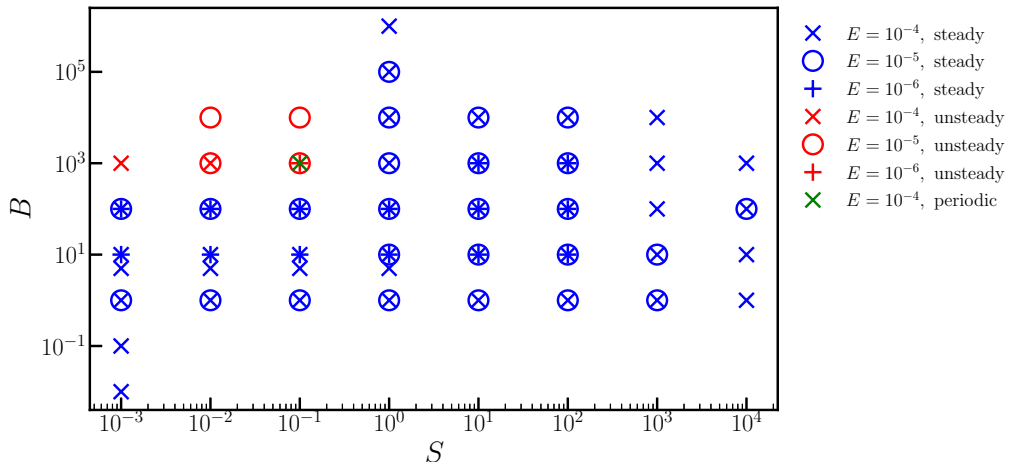


Figure 1: Stability diagram in (S, B) parameter space showing all models summarised in tables A.1 to A.3. The symbol type represents the Ekman number (crosses denote $E = 10^{-4}$, circles denote $E = 10^{-5}$ and plus signs denote $E = 10^{-6}$); the symbol colour represents the stability of the solution obtained (blue denotes a steady state solution, red denotes a time dependent solution and green denotes a periodic solution).

231 For all models, the maximum power was found at long wavelengths (the lowest l), which
 232 generally exceeded the power in the shortest wavelengths (high l) by a large amount: at
 233 least two, though usually four or five, orders of magnitude.

234 Fig. 1 is a stability diagram showing regions of parameter space resulting in steady
 235 and unsteady solutions. The figure shows the transition between high B and low S
 236 models, which are unsteady, and higher S models, which produce a steady state. One
 237 periodic model was obtained at the boundary between the steady and unsteady regions
 238 of parameter space. In the remainder of this work, we focus our attention upon the
 239 steady-state regime; time-dependent models are the subject of a future paper.

240

241 3. Results

242 Fig. 2 shows the temperature perturbations in the equatorial plane, denoted T_f^* , for
 243 models at $E = 10^{-4}$ and a range of B and S values. Note that in the remainder of this

244 text, we use T_f^* (the fluctuating part of the temperature) as a proxy for T_1^* defined in
 245 eq. (2.1). To calculate the quantity T_f^* , the Y_0^0 spherical harmonic component of the
 246 total temperature T^* has been removed, which includes all of T_0^* and also the mean
 247 of T_1^* . Therefore, T_f^* and T_1^* differ in that the former is zero mean and
 248 the latter is not. Figs 3 and 4 show the radial and azimuthal velocity components, u_r^*
 249 and u_ϕ^* , for the same models. At low B and S , the temperature fluctuations are large-
 250 scale with a Y_2^2 spatial pattern locked to the applied heat flux pattern on the outer
 251 boundary and penetrating through the whole shell depth. The two lobes of negative
 252 temperature (blue) correspond to regions of high outward heat flux and the two lobes
 253 of positive temperature (red) correspond to regions of low outward heat flux. Zeroes of
 254 T_f^* (at $\phi \approx \pi/4, 3\pi/4, 5\pi/4, 7\pi/4$) correspond to locations of the outer boundary heat
 255 flux changing sign. The radial velocity is dominated by large-scale convection cells that
 256 occupy the whole shell, with two upwellings and two downwellings present, and the peak
 257 velocity amplitudes occur at approximately half the shell radius. The lateral locations of
 258 these maxima and minima approximately correspond to locations of $T_f^* = 0$. In azimuthal
 259 velocity, locations of diverging (converging) lobes of opposite sign correspond to locations
 260 of upwellings (downwellings) of radial flow and $T_f^* = 0$.

261 As the stratification parameter (S) increases, temperature perturbations and flow
 262 magnitudes decrease and the dynamics become concentrated towards the outer boundary
 263 rather than occupying the entire shell thickness. Radial flow cells begin to elongate
 264 near the inner boundary, and high velocity magnitudes are concentrated near the outer
 265 boundary rather than the inner boundary. In u_ϕ^* , inner and outer cells of the same polarity
 266 begin to join together through tails trailing from the outermost cells, with the inner cells
 267 decreasing in amplitude. Radial flow is strongly suppressed with increasing S , which is
 268 expected because stratification does not permit large radial velocities. Azimuthal flow is

only weakly suppressed with increasing stratification as horizontal flows are permitted within a stably stratified layer. At high S , all flow becomes confined to a thin shear layer of thickness δ^* beneath the outer boundary (hereafter referred to as the ‘penetration depth’ into the fluid).

As B increases, temperature perturbations decrease and flow magnitudes increase. This is a consequence of the fixed heat flux outer boundary condition; increasing the buoyancy produces stronger flows that better homogenise the temperature, resulting in velocity increasing with B while temperature perturbations decrease (e.g. Otero *et al.* 2002; Mound & Davies 2017). Flows are phase shifted so that upwellings (and diverging u_ϕ^*) and downwellings (and converging u_ϕ^*) are now locked to the boundary pattern itself rather to locations of heat flux changing sign. Upwellings (downwellings) are beneath high (low) boundary heat flow regions. At low S and increasing B (e.g. figs 2–4, a–c), temperature and flow patterns are strikingly different from models at other parameters. Downwellings become increasingly faster and much narrower in azimuth with increasing B , though still occupying the whole shell radius, whilst the upwellings remain broad and low amplitude. This pattern of slow, broad upwellings and fast, narrow downwellings in the presence of lateral boundary anomalies was also obtained in e.g. Willis *et al.* (2007); Sreenivasan & Gubbins (2011). At higher S , upwellings and downwellings are of similar lateral extent and dynamics are confined to a thin shear layer whose thickness decreases with increasing S and B .

Fig. 5 shows u_r^* (left) and u_ϕ^* (middle) and T_f^* (right) in a meridional plane for models run at $E = 10^{-4}$ and $B = 1$ for a range of stratification parameters (S). At low S , dynamics are dominated by large-scale features that are aligned with the rotation axis. There is little variation parallel to the z -axis, as expected in a rapidly rotating system from the Taylor-Proudman theorem. As stratification increases, the dynamics are

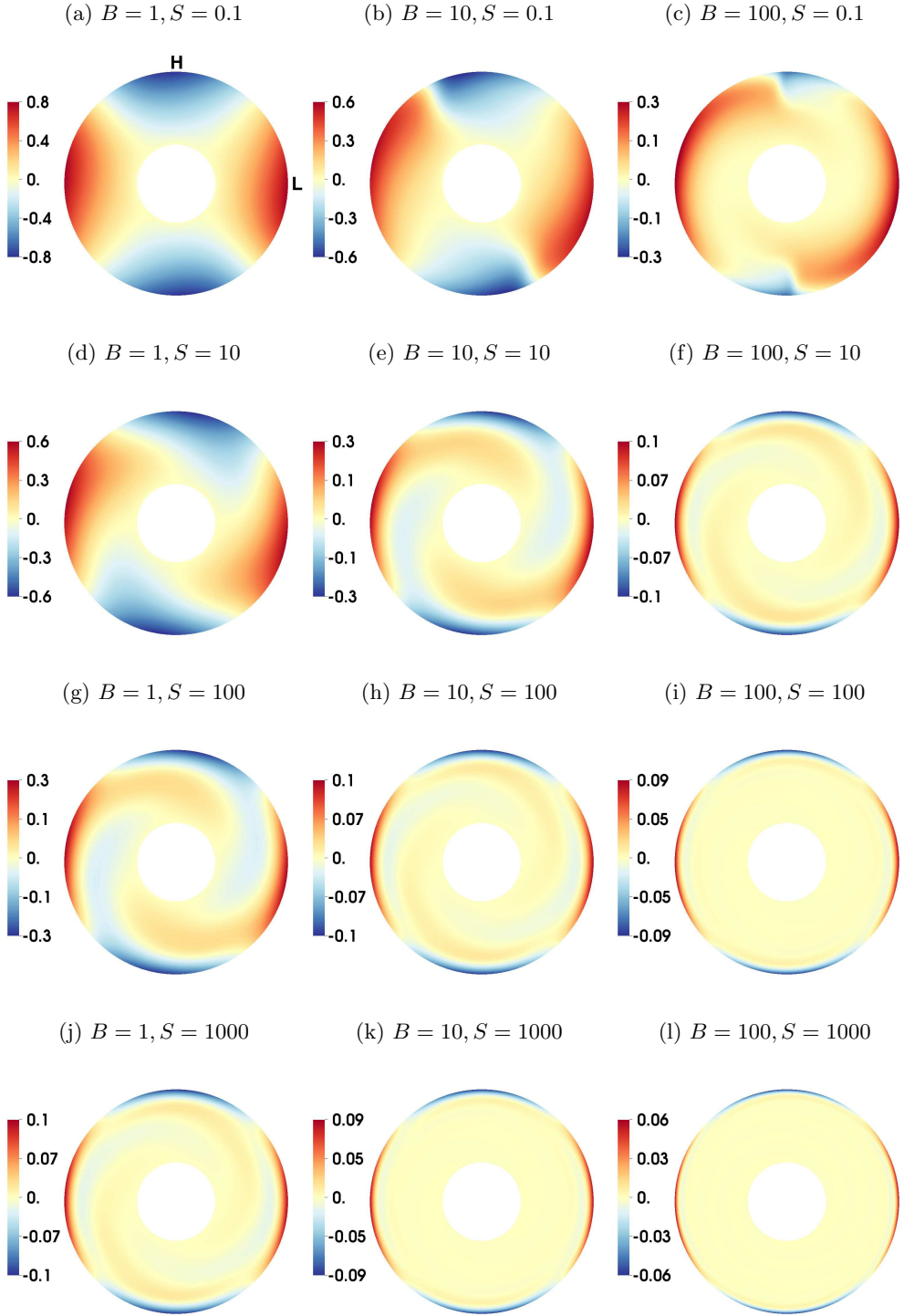


Figure 2: Equatorial plots of T_f^* for models at $E = 10^{-4}$ and varying S (increasing from top to bottom) and B (increasing from left to right). Red indicates positive values and blue indicates negative values. Note the different colour scales. Locations of high (H) and low (L) outward heat flux are shown on the top left.

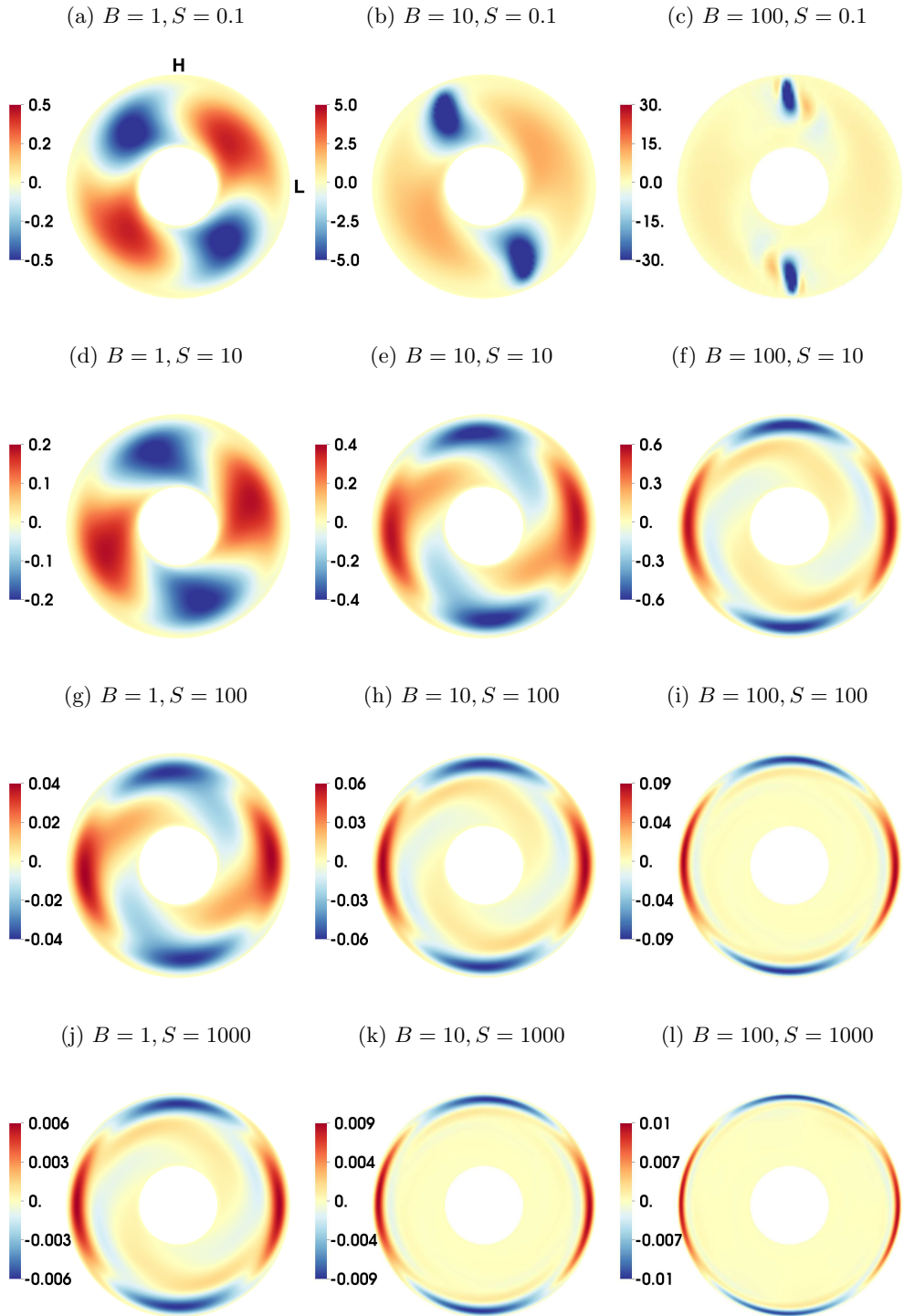


Figure 3: Equatorial plots of u_r^* for models at $E = 10^{-4}$ and varying S (increasing from top to bottom) and B (increasing from left to right). Red indicates positive values and blue indicates negative values. Note the different colour scales. Locations of high (H) and low (L) outward heat flux are shown on the top left.

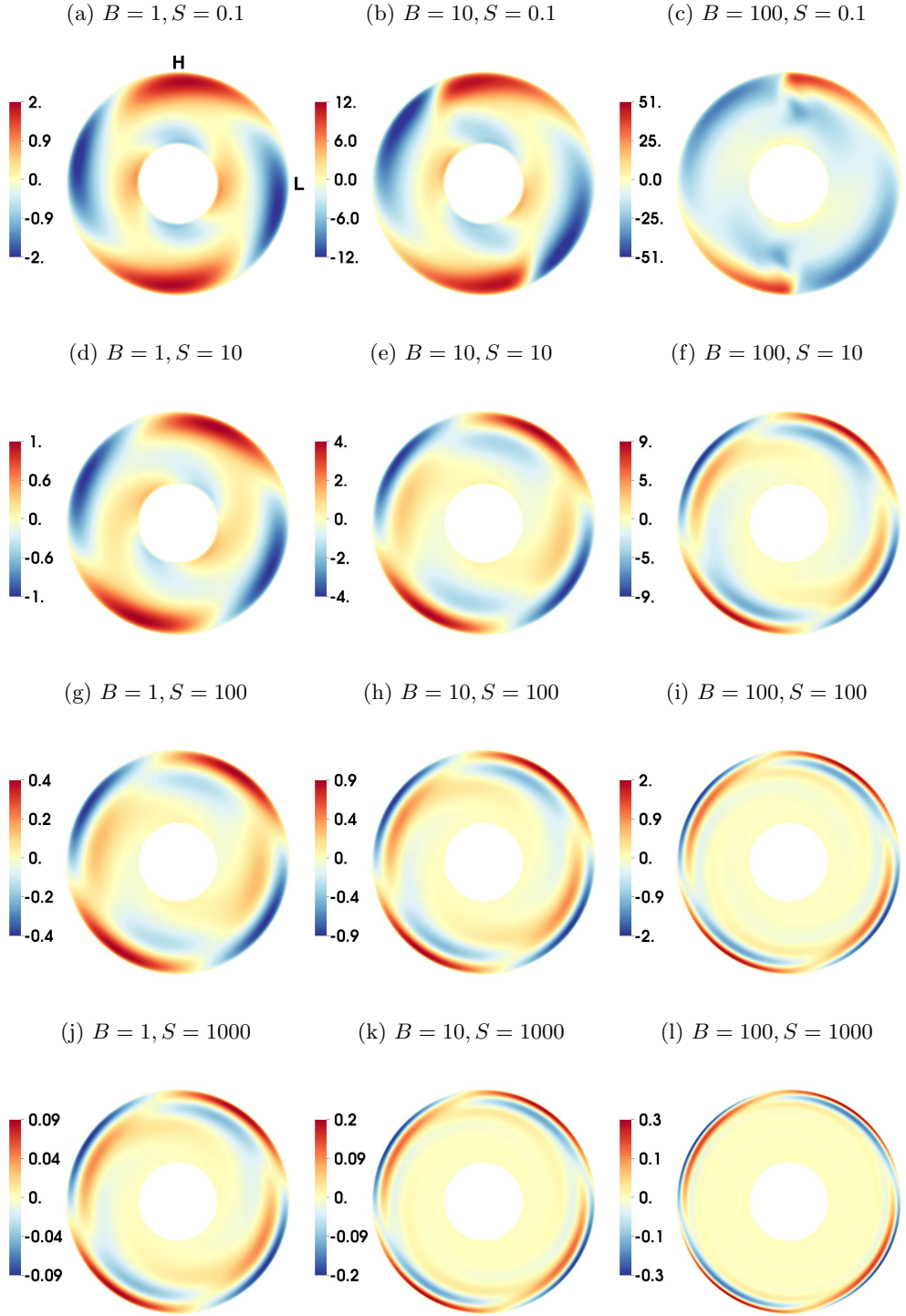


Figure 4: Equatorial plots of u_ϕ^* for models at $E = 10^{-4}$ and varying S (increasing from top to bottom) and B (increasing from left to right). Red indicates positive values and blue indicates negative values. Note the different colour scales. Locations of high (H) and low (L) outward heat flux are shown on the top left.

294 confined to the shear layer at the top of the shell, as seen in figures 2 to 4, which means
 295 that significant z variations now occur in the models on the order of the penetration
 296 depth, δ^* .

297 Fig. 6 shows $\langle u_r^* \rangle_v$, $\langle u_\phi^* \rangle_v$, $\langle v_\theta^* \rangle_v$ and $\langle T_f^* \rangle_v$, where the angular brackets denote the
 298 magnitude averaged over the shell volume V such that, for example, $\langle u_r^* \rangle_v = \int |u_r^*| dV$,
 299 and likewise for vector quantities. We define a similar operator for the integral over
 300 a surface S of radius r such that $\langle u_r^* \rangle_s = \frac{1}{S} \int |u_r^*| dS$. We adopt an average over the
 301 entire domain, rather than only the shear layer volume, because it is difficult to estimate
 302 the exact location of the shear layer edge. We assume that the quantities of interest
 303 are dominated by their values within the shear layer, with negligible contribution from
 304 elsewhere in the domain, such that our volume-averaged quantities are representative of
 305 the shear layer volume-average. Furthermore, we use the average of the modulus because
 306 integration over solid angle would otherwise result in large scale cancellation due to
 307 the spherical symmetry of the problem. The volume-averaged quantities show a clear
 308 transition from the low stratification (S) regime, in which dynamics appear to be related
 309 to B and E only, and the high S regime, in which stratification dominates the dynamics
 310 and the quantities obey power law relationships in both S and B .

311 We use the location of the peak in $\langle u_r^* \rangle_s$ as a function of radius to estimate the
 312 penetration depth, δ^* , for each model. We define the radius of maximum $\langle u_r^* \rangle_s$ as r_{\max}
 313 and calculate the penetration depth as follows

$$\delta^* = r_o - r_{\max}. \quad (3.1)$$

314 Radial velocity is used to estimate the penetration depth because it has only a single
 315 peak that is located centrally within the shear layer, whereas the horizontal components
 316 typically have several peaks, with the highest value close to the outer boundary in our

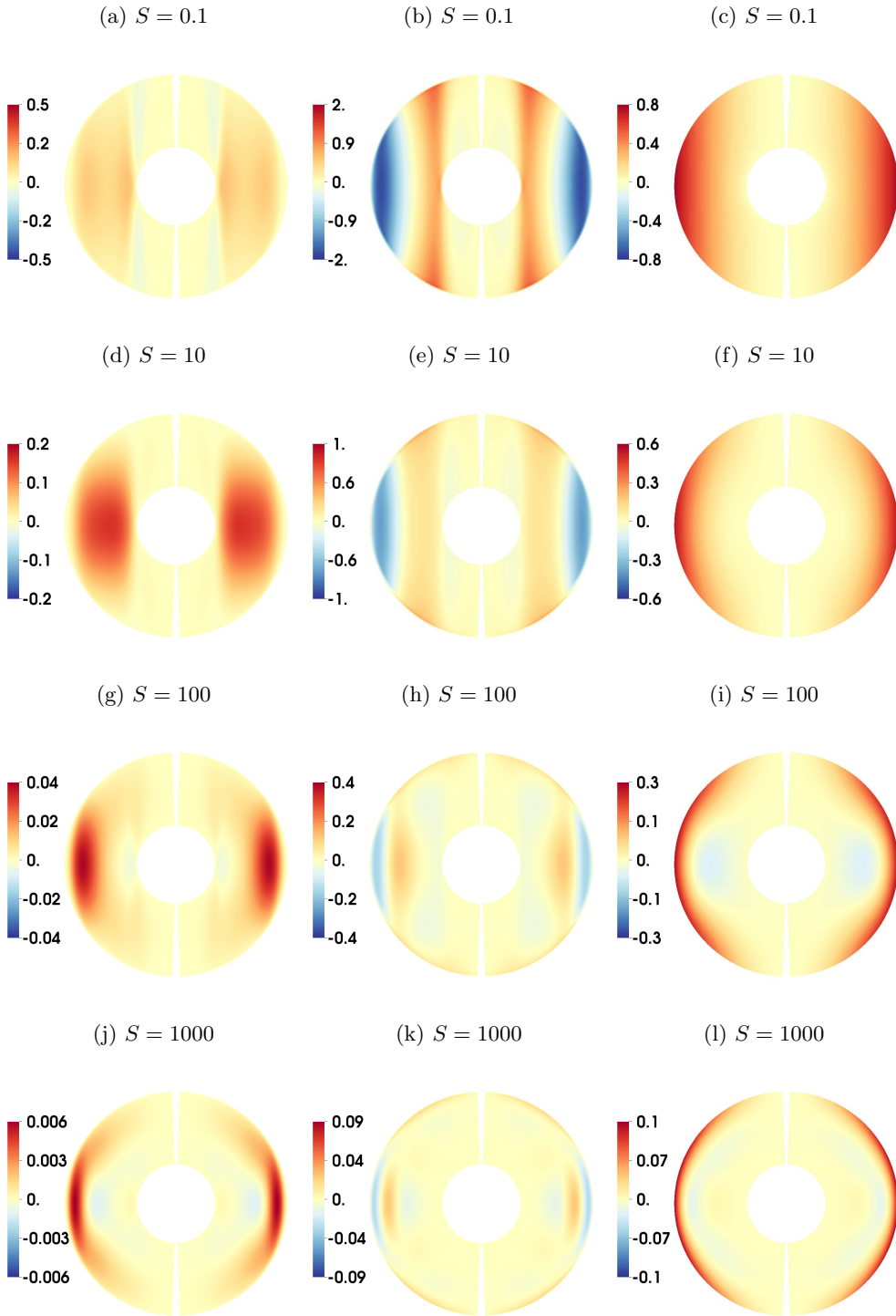
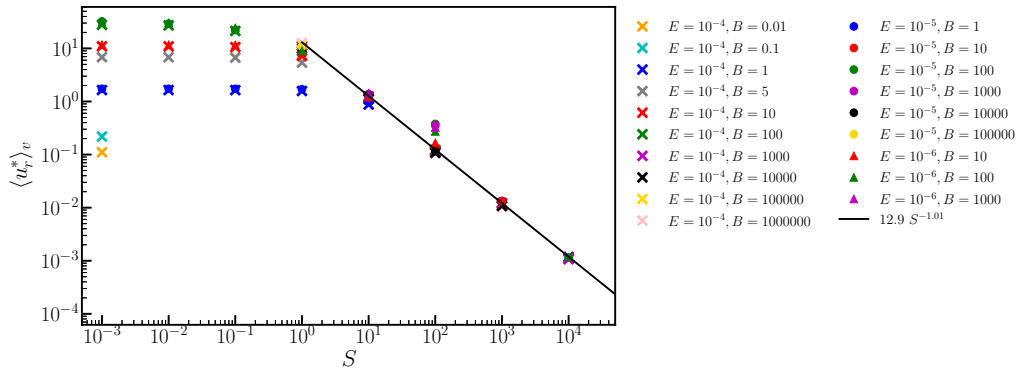
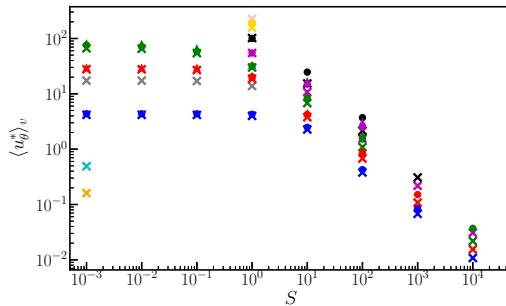


Figure 5: Meridional plots of u_r^* (left), u_θ^* (middle) and T_f^* (right) for models at $E = 10^{-4}$, $B = 1$ and varying S (increasing from top to bottom). Red indicates positive values and blue indicates negative values.

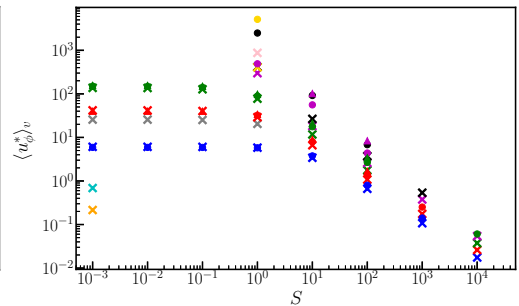
(a)



(b)



(c)



(d)

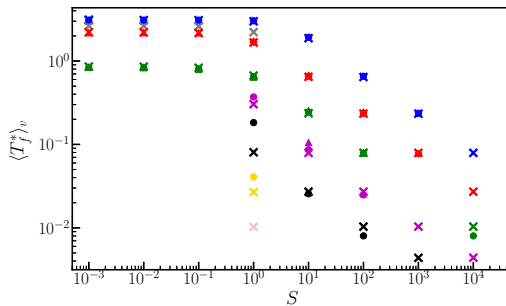


Figure 6: Volume-averaged values of the absolute (a) radial velocity, $\langle u_r^* \rangle_v$, (b) meridional velocity, $\langle u_\theta^* \rangle_v$, (c) azimuthal velocity, $\langle u_\phi^* \rangle_v$ and (d) temperature perturbations, $\langle T_f^* \rangle_v$, as a function of the stratification parameter, S , for all steady models. Symbol shapes represent the Ekman number, E , and colours represent the buoyancy parameter, B . The black line in panel (a) is the power law best fit for all models at $S > 1$.

317 $S > 1$ models, see the equatorial sections in figs 3 and 4, and fig. 7 for a representative
 318 example of radial velocity profiles. Note that the $\langle \rangle_s$ operation averages any longitudinal
 319 dependence of u_r^* , as seen in fig. 5 for example. Fig. 8 shows that δ^* has different behaviour

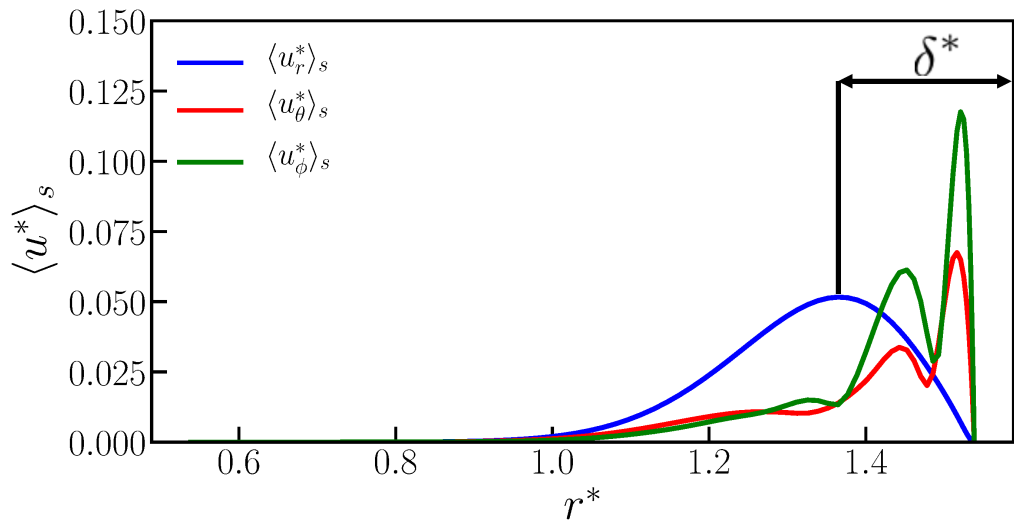


Figure 7: Components of velocity as a function of radius for a model run at $E = 10^{-4}$, $B = 100$ and $S = 1000$. The line colour denotes the flow component (blue for radial, red for meridional and green for azimuthal). The black arrow represents the width used as an estimate for the penetration depth, δ^* , in this model (calculated according to (3.1)).

320 in the two stratification (S) regimes, with δ^* on the order of the shell thickness at low S
 321 and obeying power law relationships in S and B .

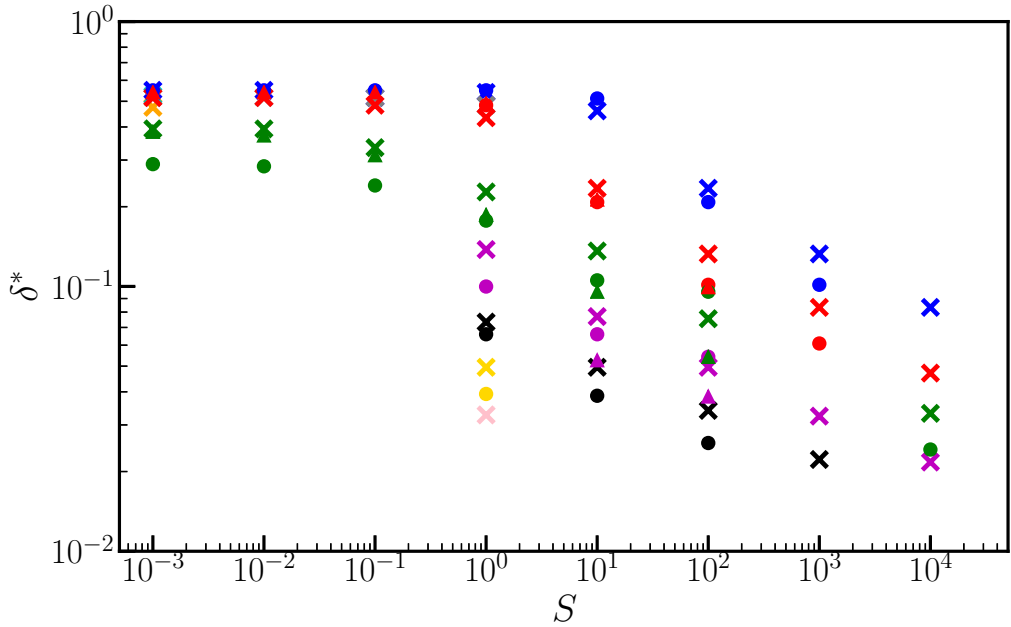


Figure 8: Estimates of the penetration depth δ^* , as a function of the stratification parameter, S , for all steady models. Symbol shapes represent the Ekman number, E , and colours represent the buoyancy parameter, B . The key is given in fig 6a.

322 4. Scaling analysis

323 In this section, our aim is to recover power laws of the form

$$f = S^a B^b \quad (4.1)$$

324 from the governing equations to express the velocity components, temperature fluctua-
 325 tions and penetration depth (denoted f above) as functions of the control parameters
 326 S and B (and, equivalently, S , $Ra_{\mathcal{H}}$ and E), where coefficients a and b are to be
 327 determined. We then verify these predicted scalings for our models using the volume
 328 averaged quantities introduced above, and finally we extrapolate the power laws to
 329 planetary core conditions.

4.1. High stratification regime

At high stratification parameter, S , flow is confined to a shear layer of thickness δ^* at the top of the shell and this penetration depth decreases with increasing stratification. Within the layer, flow tends to be in long, thin lobes with relatively little lateral variation, which suggests that the radial gradients of velocity ($\frac{\partial}{\partial r^*}$) are larger than the horizontal ($\frac{\partial}{\partial \theta}$ and $\frac{\partial}{\partial \phi}$) gradients. Our dimensionless horizontal lengths are $O(1)$ and the relevant radial length scale is $O(\delta^*)$ so that the continuity equation ($\nabla \cdot \mathbf{u}$) gives a relationship between the velocity components

$$u_r^* \sim \delta^* u_\theta^* \sim \delta^* u_\phi^*, \quad (4.2)$$

assuming that $\frac{\partial}{\partial \theta} \sim \frac{\partial}{\partial \phi}$. Adherence of our high S models to this scaling was verified using the estimates of δ^* shown in fig. 8 and volume-averaged velocities $\langle u_r^* \rangle_v$, $\langle u_\theta^* \rangle_v$ and $\langle u_\phi^* \rangle_v$ shown in fig. 6. These results, summarised in fig. B.1 show clear flattening of $\langle u_r^* \rangle_v / \delta^* \langle u_h^* \rangle_v$ for the highest S models, where $\langle u_h^* \rangle_v$ is the average volume-averaged horizontal velocity ($= \frac{1}{2} [\langle u_\theta^* \rangle_v + \langle u_\phi^* \rangle_v]$).

4.1.1. Vorticity equation balance

Taking the curl of (2.14) gives the dimensionless vorticity equation for steady flow

$$\frac{\partial \mathbf{u}^*}{\partial z^*} = \nabla \times B T_1^* \mathbf{r}^* + E \nabla^2 \boldsymbol{\omega}^*, \quad (4.3)$$

in which pressure does not appear and inertia is assumed small. In this three-term balance, we note that the buoyancy term is purely horizontal, and so the radial component of the first term must be small except outside the viscous boundary layer. Motivated by the observation that the viscous term is large only near the boundaries (fig. B.2), we seek a thermal wind balance between the horizontal components of the Coriolis and buoyancy

350 terms, and will show subsequently that the resulting scaling remains consistent for cases
 351 in which viscosity is also included in the balance.

352 We adopt δ^* as the relevant length scale in the Coriolis term that controls variations
 353 parallel to the rotation axis at high stratification (see fig. 5), and an $O(1)$ horizontal
 354 length scale for the buoyancy term since it is determined by the boundary condition.
 355 The balance is then

$$\frac{u_{\theta,\phi}^*}{\delta^*} \sim B T_1^*. \quad (4.4)$$

356 The volume-averaged magnitude of the Coriolis and buoyancy terms, scaled by our
 357 approximations to those terms using δ^* and volume-averaged velocities and temperatures
 358 ($\frac{\partial \mathbf{u}^*}{\partial z^*} \sim \langle u^* \rangle_v / \delta^*$ for Coriolis and $\nabla \times B T_1^* \mathbf{r}^* \sim B \langle T_f^* \rangle_v$ for buoyancy), are plotted for
 359 all models in figs B.3 and B.4. These ratios are approximately one for all high S models,
 360 and show little S dependence, indicating that the correct scalings are encapsulated in
 361 our approximations and that the volume-averaged quantities are suitable diagnostics of
 362 model output.

363 4.1.2. Temperature equation balance

364 The dimensionless time-independent temperature equation is

$$\nabla^2 T_1^* - u_r^* \frac{\partial T_1^*}{\partial r^*} - \frac{u_\theta^*}{r} \frac{\partial T_1^*}{\partial \theta} - \frac{u_\phi^*}{r \sin \theta} \frac{\partial T_1^*}{\partial \phi} - S u_r^* r^* = 0. \quad (4.5)$$

365 Assuming that diffusion occurs on the length scale of the penetration depth, and that
 366 the geometric factors of r and $\sin \theta$ are order unity, leaves

$$\frac{T_1^*}{\delta^{*2}} - 3 \frac{u_r^*}{\delta^*} T_1^* - S u_r^* \approx 0 \quad (4.6)$$

367 using the scaling for the velocity components of equation (4.2). For two representative
 368 high S models, $(\mathbf{u}^* \cdot \nabla) T_1^*$ is small compared to the other terms, fig. B.5. Therefore,

$$\frac{T_1^*}{\delta^{*2}} \sim S u_r^*. \quad (4.7)$$

369 is the appropriate balance. The approximation $\nabla^2 T_1^* \sim \langle T_f^* \rangle_v / \delta^{*2}$ and the term balance
 370 in the temperature equation described by (4.7) were verified for our high S models, see
 371 B.6, which shows a clear flattening of $\frac{\langle T_f^* \rangle_v}{\delta^{*2}} / S \langle u_r^* \rangle_v$ for higher stratification parameters
 372 and little dependence on B .

373 4.1.3. Power law scalings

374 Rearranging (4.7) for δ^* , eliminating u_r^* using (4.2) from the continuity equation and
 375 substituting $B T_1^* \delta^*$ for horizontal flow (from balancing $\frac{\partial \mathbf{u}^*}{\partial z^*}$ with $\nabla \times B T_1^* \mathbf{r}^*$ in (4.3)),
 376 results in a scaling for the penetration depth in terms of the control parameters

$$\delta^* \sim (S B)^{-\frac{1}{4}} \sim (S Ra_{\mathcal{H}} E)^{-\frac{1}{4}}. \quad (4.8)$$

377 We now postulate that the radial velocity u_r^* depends on S but not B as it is not
 378 directly forced by the thermal wind; it arises to conserve mass for the horizontal velocity
 379 components, which are directly forced by the boundary anomalies. Then

$$u_r^* \sim S^a, \quad (4.9)$$

380 and the horizontal flow components scale as

$$u_{\theta, \phi}^* \sim S^{a+\frac{1}{4}} B^{\frac{1}{4}}, \quad (4.10)$$

381 from (4.2). The temperature perturbations depend on both S and B

$$T_1^* \sim S^b B^c \quad (4.11)$$

382 where the exponents b and c are to be determined. From (4.7) and (4.8),

$$S^{b-a} B^c \sim \frac{T_1^*}{u_r^*} \sim \delta^{*2} S \sim S^{\frac{1}{2}} B^{-\frac{1}{2}}, \quad (4.12)$$

383 substituting (4.9) and (4.11), from which we deduce $c = -\frac{1}{2}$ and $b - a = \frac{1}{2}$. Another
 384 assumption is required in order to proceed further with the analysis. We now assume
 385 that at sufficiently high β , the boundary anomalies become unimportant so that the
 386 temperature perturbations are independent of \mathcal{H} . Then, T_1^* can only depend on the
 387 product $S B$ and, since the power of B is $-\frac{1}{2}$, the power of S ($=b$) must also be $-\frac{1}{2}$. We
 388 have now determined the exponents for the temperature fluctuations

$$T_1^* \sim (SB)^{-\frac{1}{2}} \sim (SRa_{\mathcal{H}}E)^{-\frac{1}{2}}, \quad (4.13)$$

389 radial flow

$$u_r^* \sim S^{-1}, \quad (4.14)$$

390 and horizontal flow components

$$u_{\theta, \phi}^* \sim S^{-\frac{3}{4}} B^{\frac{1}{4}} \sim S^{-\frac{3}{4}} Ra_{\mathcal{H}}^{\frac{1}{4}} E^{\frac{1}{4}}. \quad (4.15)$$

391 4.1.4. Empirical fit to models

392 In order to test the scaling laws obtained in the previous section, we computed best fits
 393 to our models using a least squares inversion of the estimates of the penetration depth
 394 and the volume-averaged velocities and temperature perturbations. We seek power laws
 395 of the form

$$\tilde{y} = \epsilon S^X B^{\zeta} \quad (4.16)$$

396 where the ‘observations’ y are model outputs, and the predictions \tilde{y} are calculated
 397 from the control parameters S and B , given the specified functional form. We take the

Quantity	Prediction	Fit to models	Fit R^2
u_r^*	S^{-1}	$S^{-1.01} B^{0.02}$	0.98
u_ϕ^*	$S^{-\frac{3}{4}} B^{\frac{1}{4}}$	$S^{-0.86} B^{0.24}$	0.97
u_θ^*	$S^{-\frac{3}{4}} B^{\frac{1}{4}}$	$S^{-0.82} B^{0.21}$	0.99
T_1^*	$S^{-\frac{1}{2}} B^{-\frac{1}{2}}$	$S^{-0.46} B^{-0.46}$	1.00
δ^*	$S^{-\frac{1}{4}} B^{-\frac{1}{4}}$	$S^{-0.21} B^{-0.22}$	0.95

Table 1: Scaling analysis and least squares inversion results for all $S > 1$ models.

398 logarithm to transform the power law problem into a linear problem such that

$$\log \tilde{y} = \log \epsilon + \chi \log S + \zeta \log B \quad (4.17)$$

399 and calculate the prefactor ϵ and exponents χ and ζ using a linear least squares inversion.

400 A summary of the predicted scaling exponents ((4.8) and (4.13)-(4.15)) and those

401 obtained from the least squares fits to all models in the stratification-dominated regime

402 ($S > 1$) is provided in table 1 for comparison. A measure of how well the models are fit

403 is given by the R^2 values (rounded to two decimal places throughout). The best fitting

404 exponents are in good agreement with those obtained in the analysis; see also figs 9a to

405 9c.

406 4.1.5. *The role of viscosity*

407 Having verified our two-term balance in the vorticity equation, we now address the

408 question of whether our scalings are also consistent when considering all three terms.

409 The additional viscous term scales as $E u^* l_\nu^{-3}$, where l_ν is a relevant length scale yet to

410 be determined.

411 The assertion that $l_\nu = \delta$ leads to $l_\nu = \delta \sim E^{1/2}$ independent of S , which as figure

412 7 demonstrates is not the case as δ has clear empirical S -dependence (see also fig. B.7,

413 which shows the ratio of the viscous term to the incorrect scaling $E u_h^* \delta^{*-3}$ as a function

414 of S for all models). Alternatively, assuming that l_ν represents a thin boundary layer

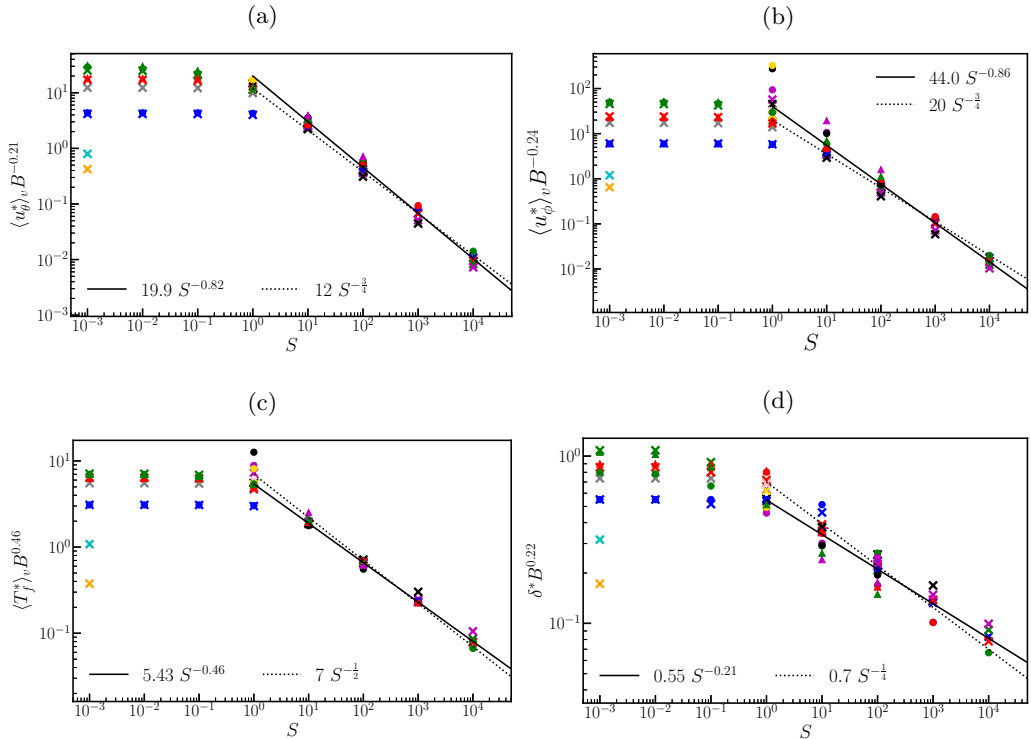


Figure 9: (a) Volume-averaged meridional velocities, (b) volume-averaged azimuthal velocities, (c) volume-averaged temperature perturbations and (d) penetration depth estimates, normalised by the best empirical fit to the buoyancy parameter for all models with $S > 1$, as a function of S . Symbol shapes represent the Ekman number, E , and colours represent the buoyancy parameter, B . The key is given in fig 6a. The solid black lines show the best fitting power laws for S in the stratification-dominated regime and the dotted lines show the theoretically predicted S exponents.

415 (consistent with figure B.2), then the three-term balance determines l_ν to be

$$l_\nu \sim (E \delta^*)^{\frac{1}{3}}. \quad (4.18)$$

416 Fig. 10 shows that the shear layer thickness (given in (4.8)) and the Ekman layer depth are
 417 comparable for most of our models, which are therefore are in fact described by a three-
 418 term (rather than a two-term) balance within the shear layer. The inclusion of viscosity
 419 within the balance in no way invalidates our analysis of the two-term scaling, but merely
 420 provides information about the characteristic lengthscale l_ν at which viscosity becomes

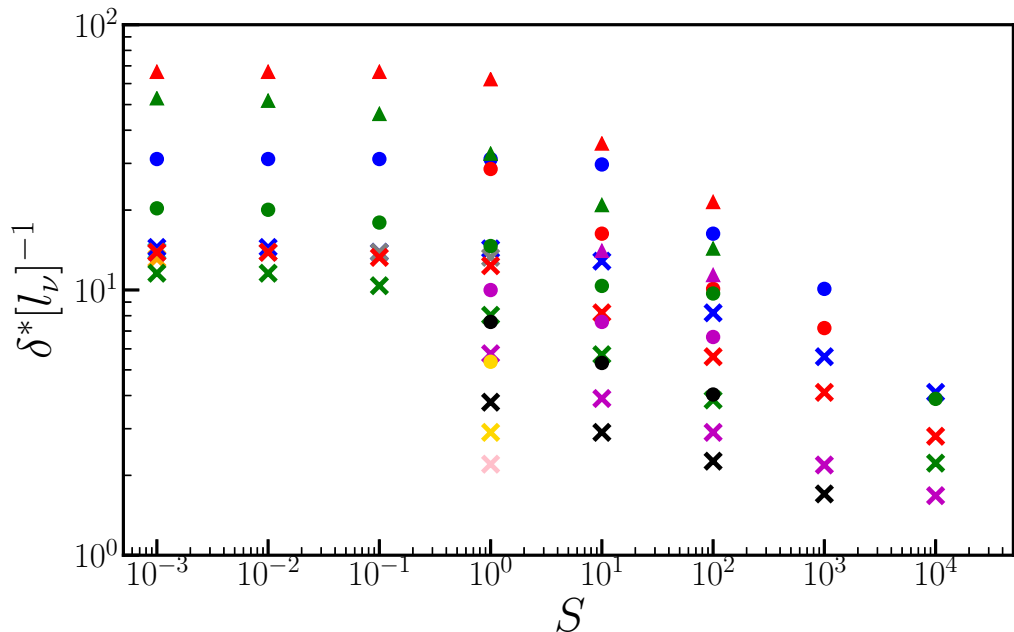


Figure 10: The shear layer thickness, δ^* , scaled by the dimensionless Ekman layer thickness estimated using (4.18) as a function of the stratification parameter, S , for all steady models. Symbol shapes represent the Ekman number, E , and colours represent the buoyancy parameter, B . The key is given in fig 6a.

421 important. Indeed, our derived scalings of the previous sections, confirmed empirically,
 422 appear to hold independently of the relative size of l_ν and δ^* . It is worth pointing out the
 423 physically relevant planetary regime is one in which $E \ll 1$ and $l_\nu \ll \delta$ (see also section
 424 5), and therefore in this limit the two term balance is appropriate for the shear-layer. We
 425 speculate that there may be a different behavioural regime in which $l_\nu \gg \delta^*$ for certain
 426 choices of parameters, when viscosity balances just one other term.

427

4.2. Low stratification regime

428

At low S , the basic state is one of neutral stability (rather than stratification) and
 429 the flow occupies the whole shell rather than being concentrated within a thin layer.

430

Furthermore, from equation (2.12) it follows also that $T_0^* \approx 0$ so that $T^* \approx T_1^*$. The

431

dynamics of the low- S regime have previously been investigated in Zhang & Gubbins

432 (1992), Gibbons & Gubbins (2000) and Gibbons *et al.* (2007), but these studies did not
 433 develop scaling laws as we do here using a much broader range of models in (E, S, B)
 434 space.

435 Within the low- S regime, we consider the energy balance of (2.14) in a steady state, by
 436 taking the inner product with \mathbf{u}^* and integrating over the volume V . Neither the Coriolis
 437 force (which is orthogonal to the flow) nor the pressure contributes to the energy equation,
 438 as the fluid is incompressible and

$$\int_V \mathbf{u}^* \cdot \nabla \hat{P} dV = \int_V \nabla \cdot (\hat{P} \mathbf{u}^*) dV = 0 \quad (4.19)$$

439 because $u_r^* = 0$ on the boundary. The balance

$$B \int_V T^* u_r^* r^* dV = E \int_V (\nabla \times \mathbf{u}^*)^2 dV \quad (4.20)$$

440 is then exact.

441 Following Shishkina *et al.* (2016), the temperature equation (2.13) in steady state and
 442 the limit of no source ($S = 0$) may be written

$$\nabla \cdot (\mathbf{u}^* T^* - \nabla T^*) = 0. \quad (4.21)$$

443 Integrating over the volume bounded by radii r^* and r_o , with $r^* < r_o$, and using the
 444 divergence theorem leads to

$$\langle u_r^* T^* - \frac{\partial T^*}{\partial r^*} \rangle = 0 \quad (4.22)$$

445 at any radius r^* , where $\langle \cdot \rangle$ denotes integration over all solid angle, and where we have
 446 used the facts that both u_r^* and $\langle \frac{\partial T^*}{\partial r^*} \rangle = \langle Y_2^2 \rangle = 0$ at $r^* = r_o$. It follows that

$$\int_V T^* u_r^* r^* dV = \int_{r_i}^{r_o} r^{*3} \langle u_r^* T^* \rangle dr^* = \langle \int_{r_i}^{r_o} r^{*3} \frac{\partial T^*}{\partial r^*} dr^* \rangle, \quad (4.23)$$

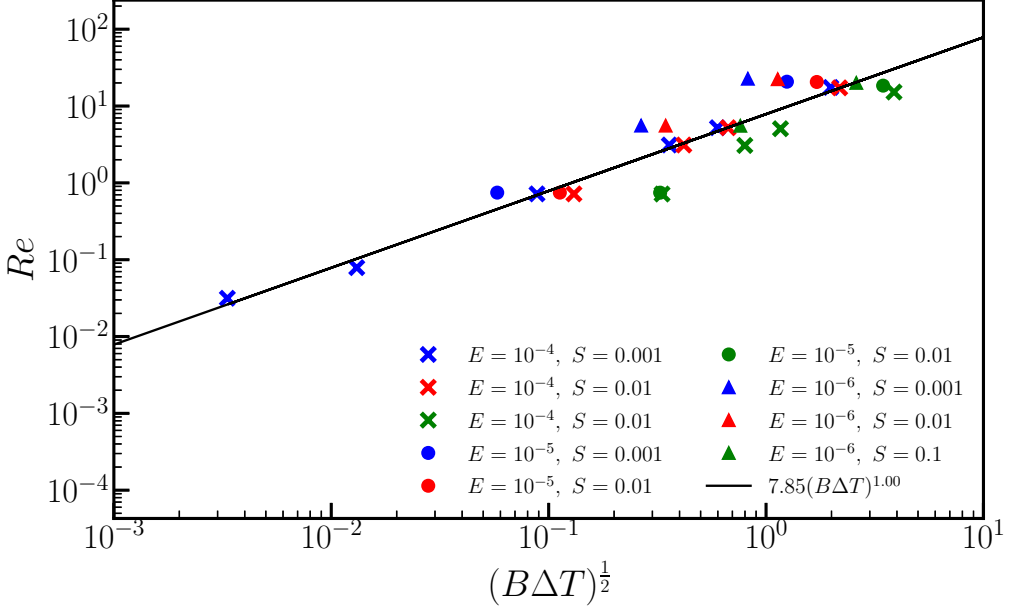


Figure 11: The Reynolds number Re against $(B\Delta T)^{\frac{1}{2}}$ for all low- S models. The black line shows the best empirical fit to the simulations.

447 and integrating by parts leads to

$$[\langle T^* \rangle [r^{*3} - 3r^{*2} + 6r^* - 6]]_{r_i}^{r_o} = A(r_o) \Delta T \quad (4.24)$$

448 because $T^* = 0$ on $r^* = r_i$, where $A = r_o^3 - 3r_o^2 + 6r_o - 6$ is a constant and $\Delta T = \langle T^* \rangle|_{r_o}$.

449 The exact relation

$$BA \Delta T = E \int_V (\nabla \times \mathbf{u}^*)^2 dV \quad (4.25)$$

450 then follows. The viscous dissipation term on the right hand side may be estimated as

451 $(u^*)^2$ by assuming a viscous boundary layer length scale of $E^{1/2}$. The resulting scaling

$$u^* \sim \sqrt{B\Delta T} \quad (4.26)$$

452 is verified using an empirical fit to the low- S models, which gives $Re \sim (B\Delta T)^{0.50}$

453 ($R^2 = 0.88$) and is shown in fig. 11.

454 We now need to estimate ΔT , which is not prescribed in models with a fixed heat flux

455 boundary condition, in contrast to those with a fixed temperature boundary condition.

456 We consider the thermal dissipation equation, obtained by multiplying equation (2.13)

457 with T^* and integrating over V :

$$\int_V T^* \nabla^2 T^* dV = \frac{1}{2} \int_V (\mathbf{u}^* \cdot \nabla) T^{*2} dV = 0 \quad (4.27)$$

458 since u_r^* is zero on the boundaries, and so

$$\langle T^* \frac{\partial T^*}{\partial r^*} \rangle \Big|_{r^*=r_o} = \int_V \nabla \cdot (T^* \nabla T^*) dV = - \int_V (\nabla T^*)^2 dV \quad (4.28)$$

459 because $T^* = 0$ on the lower radial boundary. Since $\frac{\partial T^*}{\partial r^*}$ is prescribed as Y_2^2 on r_o , this

460 suggests the leftmost term is comparable to ΔT . In the rightmost term, we estimate

461 $\nabla T^* \sim \Delta T$, which is reasonable if the majority of the dissipation occurs on the lateral

462 length scale of $O(1)$. Assuming that most of the dissipation occurs over a radial length

463 scale L_T at the top of the shell, the whole term is estimated to be $(\Delta T)^2 L_T$. Thus the

464 balance in (4.28) is $\Delta T \sim (\Delta T)^2 L_T$ or

$$L_T \sim \Delta T^{-1}. \quad (4.29)$$

465 Furthermore, balancing advection (which is dominated by horizontal gradients with

466 length scales of $O(1)$) and diffusion in the temperature equation (2.13) over the length

467 scale L_T leads to $u^* \sim L_T^{-2}$. Hence $\Delta T \sim (u^*)^{1/2}$ and it therefore follows that

$$u^* \sim B^{2/3} \quad (4.30)$$

468 and

$$\Delta T \sim B^{1/3}. \quad (4.31)$$

469 The scaling for u^* is confirmed with an empirical fit to the low- S simulations, which gives

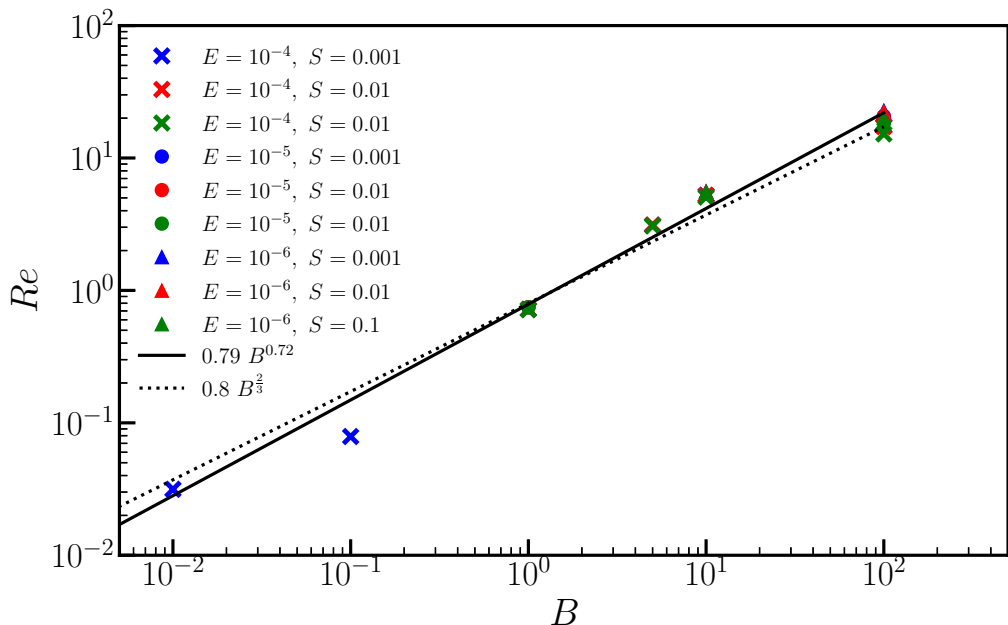


Figure 12: The Reynolds number Re against the buoyancy parameter B for all low- S models. The solid black line shows the best empirical fit to the simulations and the dotted line shows the theoretically predicted exponent from (4.30).

470 $Re \sim B^{0.72}$ ($R^2 = 0.98$) and is shown in fig 12. It is worth noting that the exponent (of
 471 $2/3$) in the scaling for u^* is higher than any of those reported in table 1 of Shishkina *et al.*
 472 (2016) for the related study of plane layer horizontal convection with lateral temperature
 473 variations on the lower boundary.

474 4.3. Effects of the shell aspect ratio

475 We have used an aspect ratio $\eta = 0.35$ in all previous models, however as we would
 476 like to apply the derived scaling laws to other shells with different aspect ratios, we
 477 now consider whether varying the geometry influences the results. To this end, we have
 478 run simulations with $\eta = 0.01$ using the parameters listed in table A.4 and obtained
 479 steady-state solutions. It is apparent that the overall dynamics of the low aspect ratio
 480 models is very similar to the previously presented models, fig. C.1. We again have two
 481 stratification regimes, a low S regime in which dynamics occupy the entire shell and

buoyancy is the dominant effect, and a high S regime in which stratification dominates and dynamics are concentrated towards the outer boundary. In both regimes, the phase of the velocity and temperature lobes with respect to the boundary anomaly pattern is the same as in the previously discussed models. We have computed the best empirical fits to the high S models in this geometry (shown in fig. 13) and confirm that these models obey the same scaling laws as derived in 4.1.3. Note that the values of the quantities shown in figures C.1 and 13, are different from those shown in previous sections for the same apparent parameter values because the length scales in the parameters S and B differ because $d = r_o - r_i = r_o(1 - \eta)$, and averaging takes place over different volumes, meaning that for example, $B = 1$ and $St = 1000$ models at $\eta = 0.35$ and $\eta = 0.01$ are not directly comparable without accounting for geometric factors. It is worth remarking that the theoretical scaling for the horizontal velocity components (which scale as $\sim S^{-3/4}$) actually agree slightly better with the numerics in the quasi-full sphere than the spherical shell calculations, indicating a possible weak dependence on r_i for such quantities.

5. Application of scaling laws to planetary cores

In order to apply our power law scalings to a planet, we must estimate S and B for its outer core. We write β and \mathcal{H} in terms of temperature gradients at the CMB

$$\beta d = \left. \frac{dT_{ad}}{dr} \right|_{r_o} - \left. \frac{dT_c}{dr} \right|_{r_o} \quad (5.1)$$

where T_{ad} is the adiabatic temperature and T_c is the core temperature at the CMB, and

$$\mathcal{H} = \left. \frac{dT'}{dr} \right|_{r_o} = \frac{q'}{k_c}, \quad (5.2)$$

where T' (q') is the anomalous temperature (heat flow per unit area) on the core-side of the CMB. In equation (5.2), we have used the continuity of heat-flux across the CMB

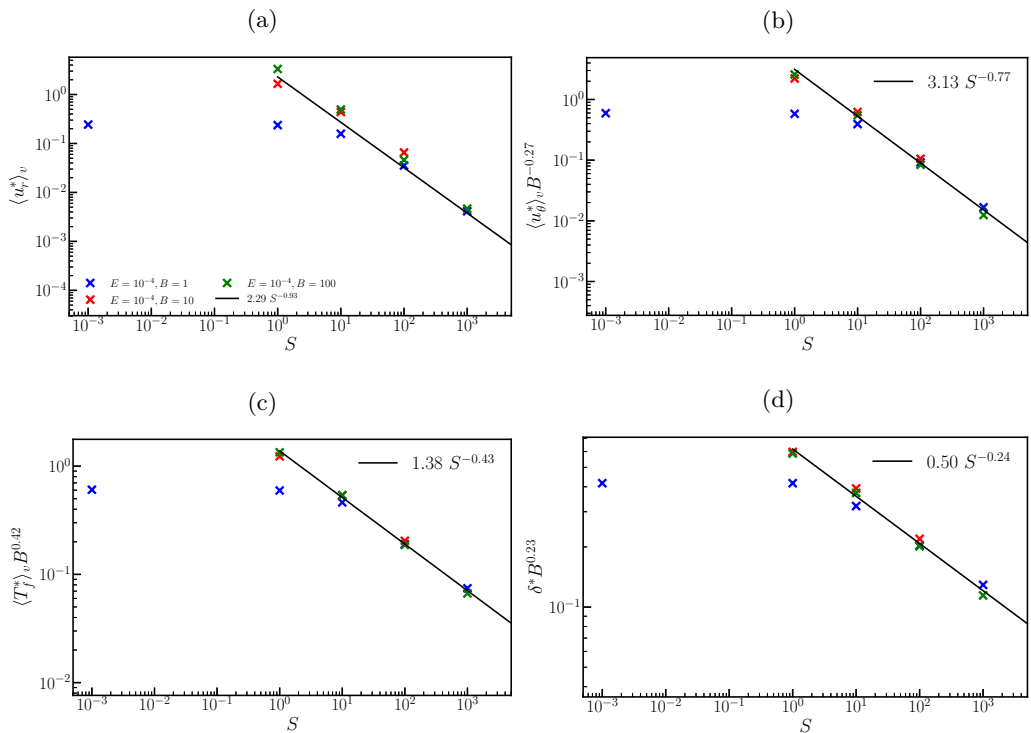


Figure 13: (a) Volume-averaged radial velocities, (b) volume-averaged azimuthal velocities, (c) volume-averaged temperature perturbations and (d) penetration depth estimates, normalised by the best empirical fit to the buoyancy parameter for all models with $\eta = 0.01$ and $S > 1$, as a function of S . The R^2 values for the fits are, respectively, 0.95, 0.99, 1.00 and 0.99. Symbol shapes represent the Ekman number, E , and colours represent the buoyancy parameter, B . The black line shows the best fitting power law in S for models at $S > 1$.

502 along with its estimated value, q' , on the mantle-side; k_c is the thermal conductivity of
 503 the core. The gradients in (5.1) are evaluated using

$$\left. \frac{dT_{ad}}{dr} \right|_{r_o} = \frac{\alpha_T g_c T_c}{C_p} \quad (5.3)$$

504 and

$$\left. \frac{dT_c}{dr} \right|_{r_o} = \frac{Q_{cmb}}{A_{cmb} k_c} \quad (5.4)$$

505 where g_c is the acceleration due to gravity at the CMB, C_p is the core specific heat, Q_{cmb}
 506 is the total CMB heat flux, A_{cmb} is the area of the CMB ($=4\pi r_o^2$) and k_c is the core

507 thermal conductivity. For the Earth’s core, we have taken a range of plausible values from
 508 the literature, given in table 2, and calculated a range of possible S and B parameters.
 509 Estimating the stratification parameter ($S = \beta d/\mathcal{H}$) is particularly challenging due to
 510 large uncertainties on \mathcal{H} , the magnitude of lateral variations in CMB heat flux, whose
 511 estimate derives from relating observed shear-wave anomalies with either thermal or
 512 chemical heterogeneities. If the anomalies are attributed predominantly to thermal
 513 differences in the mantle, then the value of q' from table 2 leads to S values of $O(10^{-6})$
 514 to $O(10^{-4})$ and B values of $O(10^{17})$, placing the core in a regime in which the stratified
 515 layer is likely penetrated by unsteady boundary-driven flow.

516 On the other hand, if the mantle heterogeneities are attributed instead to chemical
 517 anomalies (e.g. Garnero *et al.* 2016; Lau *et al.* 2017), then \mathcal{H} could be much smaller
 518 than the above estimate, rendering S plausibly $O(1)$ or above, placing the core in the
 519 stratification-dominated regime. Taking $S = 1$ for illustration with our estimates of B ,
 520 applying the high S scalings (4.13) to (4.15) gives dimensional temperature perturbations
 521 of $O(10^{-3}$ K), radial velocities of $O(10^{-12}$ m s $^{-1}$), horizontal velocities of $O(10^{-7}$ m s $^{-1}$)
 522 and penetration depths of around 70 m, much thicker than the estimated viscosity
 523 boundary layer in Earth’s core of about 1 m (e.g. Livermore *et al.* 2016) associated
 524 with $E = 10^{-15}$. A similar analysis for Ganymede’s core, using values from table 1
 525 of Rückriemen *et al.* (2015) and estimating $\alpha_T = 5.8 \times 10^{-5}$ based on Williams &
 526 Nimmo (2004), gives B values of $O(10^{13})$ and S values of $O(10^{-1})$ to $O(1)$, assuming
 527 the mantle heterogeneities are attributed to thermal anomalies. As for the Earth, if the
 528 anomalies are predominantly due to chemical sources, these S values are significantly
 529 underestimated and Ganymede’s core will be in the stratified regime.

530 For comparison with other works on stratified fluids, it is of interest to calculate the

531 Brunt-Väisälä frequency, N , defined by

$$N^2 = -\frac{g}{\rho_0} \frac{\partial \rho'}{\partial r} \quad (5.5)$$

532 both for our models and for the planetary interiors considered. Non-dimensionalising
 533 with the same scalings as used previously gives the ratio of the Brunt-Väisälä frequency
 534 to the rotation rate

$$\frac{N}{2\Omega} = \sqrt{\frac{B E}{Pr} \frac{\partial T^*}{\partial r^*}} = \sqrt{\frac{B E S}{Pr}}, \quad (5.6)$$

535 assuming $\frac{\partial T^*}{\partial r^*} \approx \frac{\partial T_0^*}{\partial r^*}$ due to the small magnitudes of the temperature perturbations.

536 Values of this ratio for our simulations vary between $O(10^{-6})$ and $O(10)$, given in
 537 tables A.1 to A.4 in appendix A. Based on our $B-S$ estimates for Earth and Ganymede,
 538 along with E and Pr estimates from table 1 of Schaeffer *et al.* (2017) for Earth ($E =$
 539 10^{-15} , $Pr = 0.1 - 10$) and table 4 of Schubert & Soderlund (2011) for Ganymede ($E =$
 540 10^{-13} , $Pr = 0.1$), we estimate their Brunt-Väisälä ratios of $O(1)$ for some parameter
 541 combinations, consistent with other estimates using different methods (e.g. Buffett 2014).
 542 Ignoring the dependence on E , it is worth remarking that the relationship between N and
 543 the product SB may explain why this quantity is so important in our derived theoretical
 544 scalings, with $\delta^* \sim N^{-1/4}$ and $T_1^* \sim N^{-1/2}$.

Parameter	Symbol	Value	Reference
Inner core radius	r_i	1221 km	Dziewonski & Anderson (1981)
Outer core radius	r_o	3480 km	Dziewonski & Anderson (1981)
Shell thickness	$d (= r_o - r_i)$	2259 km	Dziewonski & Anderson (1981)
Gravitational acceleration constant at CMB	g_c	10.68 ms^{-2}	Olson (2009)
Angular velocity of rotation	Ω	$7.272 \times 10^{-5} \text{ s}^{-1}$	Olson (2009)
Coefficient of thermal expansion	α_T	$1.5 \times 10^{-5} \text{ K}^{-1}$	Gubbins <i>et al.</i> (2003)
Core thermal diffusivity	κ	$1.25 \times 10^{-5} \text{ m}^2 \text{ s}^{-1}$	Pozzo <i>et al.</i> (2012)
Core thermal conductivity	k_c	$100 \text{ W m}^{-1} \text{ K}^{-1}$	Pozzo <i>et al.</i> (2013)
Lower mantle thermal conductivity	k_m	$10 \text{ W m}^{-1} \text{ K}^{-1}$	Ammann <i>et al.</i> (2014)
Core specific heat capacity	C_p	$728 \text{ J kg}^{-1} \text{ K}^{-1}$	Gubbins <i>et al.</i> (2003)
CMB temperature	T_c	4000 K	Olson (2009)
Total CMB heat flow	Q_{cmb}	5 TW to 17 TW	Lay <i>et al.</i> (2008); Nimmo (2015)
Total adiabatic heat flow	Q_{ad}	14 TW to 16 TW	Pozzo <i>et al.</i> (2012)
Peak-to-peak anomalous CMB heat flow	q'	100 mWm^{-2} to 300 mWm^{-2}	Nakagawa & Tackley (2013)

Table 2: Outer core and lower mantle physical, thermodynamics and transport properties used to estimate S and B for the Earth.

6. Discussion and conclusions

We have investigated a thermally stratified fluid in a rotating spherical shell subject to a laterally varying heat flux pattern on the outer boundary. Converged, steady-state numerical simulations were obtained for $Pr = 1$, $E = 10^{-6}$ to $E = 10^{-3}$, $S = 10^{-3}$ to $S = 10^4$ and $B = 10^{-2}$ to $B = 10^6$. For some parameters, we obtained time-dependent solutions, which were not analysed in this study, however we were able to map the stability domain in parameter space in greater detail than any previous study. The steady-state solutions separate into two distinct dynamical regimes corresponding to low stratification parameter (S), in which buoyancy effects dominate the dynamics, and high S , in which stratification effects dominate.

In the low S regime, the inhomogeneous thermal boundary condition drives flows that are locked to the boundary pattern and penetrate most of the shell thickness. We have developed scaling relationships for the characteristic velocity Re and the temperature drop ΔT as a function of the buoyancy parameter B . In the high S regime, stratification strongly suppresses radial flow but horizontal flow is less affected. All flow is concentrated toward the outer boundary, resulting in shear layers whose thickness decreases with increasing B and S . This layer thickness represents the depth to which the boundary driven flows penetrate the stratified fluid. We have developed scaling relations for the velocity components, temperature perturbations and penetration depth as functions of the control parameters E , B and S ; these are summarised in table 1. We have used these scaling relationships to extrapolate to Earth's core using a range of plausible parameters. If the Earth's mantle heterogeneities are attributed to thermal anomalies, the outer core is in the buoyancy-dominated regime and no steady-state solutions exist. In that case, it is likely that unsteady boundary-driven flows can penetrate the stratified layer. On the other hand, if such heterogeneities are linked to chemical anomalies (e.g. Garnero

570 *et al.* 2016; Lau *et al.* 2017), the much reduced heat-flux boundary condition would likely
571 place Earth’s core in the stratification-dominated regime where penetration from steady
572 boundary-driven flows is not possible. In that case, the shear layer thickness (i.e. the
573 depth of penetration of boundary driven flows through the core) is very small (on the
574 order of a few tens of metres) compared to the stable layer thickness and the predicted
575 velocities are several orders of magnitude smaller than those inferred from inversions
576 of geomagnetic secular variation (e.g. Holme 2015). Since there is no reason why the
577 ‘observed’ flows have to be generated (even in part) by mantle heterogeneities, the high
578 S scalings suggest that we observe general convective flow rather than boundary-driven
579 flow. Furthermore, it seems unlikely that chemical anomalies in the lowermost mantle
580 are able to directly affect the magnetic field that is generated inside the core (by creating
581 persistent non-zonal features for example) through steady boundary-driven flows.

582 However, the relative contributions of thermal and chemical anomalies to the bound-
583 ary forcing is poorly constrained for Earth and not at all for other bodies (including
584 Ganymede), hence the difficulty in estimating \mathcal{H} and the resulting uncertainty as to which
585 stratification regime their outer cores belong. Interestingly, this means that independent
586 evidence of penetrating flow within the stable layer, for example through the magnetic
587 signature of upwellings and patches of reversed magnetic flux (Gubbins 2007; Metman
588 *et al.* 2018), may be able to discriminate between these two regimes and therefore
589 offer evidence that constrains the heat-flux on the boundary, and therefore mantle
590 composition.

591 Finally, we have considered steady-state solutions in entirely stratified spherical shells
592 with no convection or magnetic field generation; further work is needed to investigate the
593 effects of adding these dynamics to our simplified models. The fluid dynamics problem
594 studied here should be relevant in the uppermost region of the outer core, where no

595 convection is expected due to stratification. Yet, it is possible that at sufficiently high
596 B , models at $S = 1$ (the lowest stratification parameter required for our high S scalings
597 to be applicable, and a plausible value for Earth's outer core) will be unsteady rather
598 than steady. This transition may well occur at a B lower than our estimates for Earth's
599 core, however, computational limitations have prevented us from reaching this transition
600 and our simulations remain many orders of magnitude from Earth estimates. Since our
601 systematic parameter study has revealed the different dynamical regimes that exist in
602 the absence of internal convection, future studies will be able to benchmark against
603 the present results and also target particular regions of parameter space to make most
604 effective use of available computational resources.

605 We thank three anonymous referees for comments and suggestions that helped to
606 improve the manuscript. This study was initiated by J.S. as his final year undergraduate
607 project. G.A.C. was supported by NERC grant NE/M012190/1, C.J.D. is supported by
608 a NERC Independent Research Fellowship (NE/L011328/1) and P.W.L. was partially
609 supported by NERC grant NE/G014043/1. This work was undertaken on ARC2, part
610 of the High Performance Computing facilities at the University of Leeds, UK. Contour
611 plots were produced in VisIt (Childs *et al.* 2012), using scripts written by Jon Mound.
612 Other figures were produced using Python's Matplotlib (Hunter 2007).

REFERENCES

- 613 AMIT, HAGAY, CHOBLET, GAËL, OLSON, PETER, MONTEUX, JULIEN, DESCHAMPS, FRÉDÉRIC,
614 LANGLAIS, BENOIT & TOBIE, GABRIEL 2015 Towards more realistic core-mantle boundary
615 heat flux patterns: a source of diversity in planetary dynamos. *Progress in Earth and
616 Planetary Science* **2** (1), 26.
- 617 AMMANN, MICHAEL W, WALKER, ANDREW M, STACKHOUSE, STEPHEN, WOOKEY, JAMES,
618 FORTE, ALESSANDRO M, BRODHOLT, JOHN P & DOBSON, DAVID P 2014 Variation of

- 619 thermal conductivity and heat flux at the Earth's core mantle boundary. *Earth Planet.*
620 *Sci. Lett.* **390**, 175–185.
- 621 AURNOU, JONATHAN M & AUBERT, JULIEN 2011 End-member models of boundary-modulated
622 convective dynamos. *Physics of the Earth and Planetary Interiors* **187** (3), 353–363.
- 623 BUFFETT, BRUCE 2014 Geomagnetic fluctuations reveal stable stratification at the top of the
624 Earth's core. *Nature* **507** (7493), 484–487.
- 625 BUFFETT, BRUCE A & SEAGLE, CHRISTOPHER T 2010 Stratification of the top of the core due
626 to chemical interactions with the mantle. *Journal of Geophysical Research: Solid Earth*
627 **115** (B4).
- 628 CHANDRASEKHAR, S. 1961 *Hydrodynamic and hydromagnetic stability*. OUP.
- 629 CHILDS, HANK, BRUGGER, ERIC, WHITLOCK, BRAD, MEREDITH, JEREMY, AHERN, SEAN,
630 PUGMIRE, DAVID, BIAGAS, KATHLEEN, MILLER, MARK, WEBER, GUNTHER H,
631 KRISHNAN, HARI & OTHERS 2012 Visit: An end-user tool for visualizing and analyzing very
632 large data. *Tech. Rep.*. Ernest Orlando Lawrence Berkeley National Laboratory, Berkeley,
633 CA (US).
- 634 CHRISTENSEN, ULRICH R. 2006 A deep dynamo generating Mercury's magnetic field. *Nature*
635 **444** (7122), 1056–1058.
- 636 CHRISTENSEN, ULRICH R. & WICHT, JOHANNES 2008 Models of magnetic field generation in
637 partly stable planetary cores: Applications to Mercury and Saturn. *Icarus* **196** (1), 16 –
638 34.
- 639 DAVIES, C.J., GUBBINS, D. & JIMACK, P.K. 2009 Convection in a rapidly rotating spherical
640 shell with an imposed laterally varying thermal boundary condition. *J. Fluid Mech.* **641**,
641 335–358.
- 642 DAVIES, CHRISTOPHER, POZZO, MONICA, GUBBINS, DAVID & ALFÈ, DARIO 2015 Constraints
643 from material properties on the dynamics and evolution of Earth's core. *Nature Geoscience*
644 .
- 645 DAVIES, CHRISTOPHER J., GUBBINS, DAVID & JIMACK, PETER K. 2011 Scalability of
646 pseudospectral methods for geodynamo simulations. *Concurrency and Computation:
647 Practice and Experience* **23** (1), 38–56.

- 648 DZIEWONSKI, A.M. & ANDERSON, D.L. 1981 Preliminary reference Earth model. *Phys. Earth*
649 *Planet. Int.* **25**, 297–356.
- 650 DZIEWONSKI, ADAM M, LEKIC, VEDRAN & ROMANOWICZ, BARBARA A 2010 Mantle anchor
651 structure: an argument for bottom up tectonics. *Earth and Planetary Science Letters*
652 **299** (1-2), 69–79.
- 653 GARNERO, EDWARD J, MCNAMARA, ALLEN K & SHIM, SANG-HEON 2016 Continent-sized
654 anomalous zones with low seismic velocity at the base of Earth’s mantle. *Nature*
655 *Geoscience* **9** (7), 481.
- 656 GIBBONS, SJ, GUBBINS, D & ZHANG, K 2007 Convection in rotating spherical fluid shells
657 with inhomogeneous heat flux at the outer boundary. *Geophysical and Astrophysical Fluid*
658 *Dynamics* **101** (5-6), 347–370.
- 659 GIBBONS, S. J. & GUBBINS, D. 2000 Convection in the Earth’s core driven by lateral variations
660 in the core-mantle boundary heat flux. *Geophys. J. Int.* **142**, 631–642.
- 661 GUBBINS, D. 2007 Geomagnetic constraints on stratification at the top of Earth’s core. *EPS*
662 **59** (7), 661–664.
- 663 GUBBINS, D., ALFÈ, D., DAVIES, C. & POZZO, M. 2015 On core convection and the geodynamo:
664 Effects of high electrical and thermal conductivity. *Phys. Earth Planet. Int.* **247**, 56–64.
- 665 GUBBINS, D., ALFÈ, D., MASTERS, G., PRICE, D. & GILLAN, M. J. 2003 Can the Earth’s
666 Dynamo run on Heat alone? *Geophys. J. Int.* **155** (2), 609–622.
- 667 GUBBINS, D & DAVIES, CJ 2013 The stratified layer at the core–mantle boundary caused by
668 barodiffusion of oxygen, sulphur and silicon. *Physics of the Earth and Planetary Interiors*
669 **215**, 21–28.
- 670 GUBBINS, D., WILLIS, A. P. & SREENIVASAN, B. 2007 Correlation of Earth’s magnetic field
671 with lower mantle thermal and seismic structure. *Phys. Earth Planet. Int.* **162**, 256–260.
- 672 HOLME, R. 2015 Large-Scale Flow in the Core. in *Treatise on Geophysics, Ed. G. Schubert* **8**,
673 91–113.
- 674 HUNTER, JOHN D 2007 Matplotlib: A 2D graphics environment. *Computing In Science &*
675 *Engineering* **9** (3), 90–95.
- 676 LAU, HARRIET CP, MITROVICA, JERRY X, DAVIS, JAMES L, TROMP, JEROEN, YANG,

- 677 HSIN-YING & AL-ATTAR, DAVID 2017 Tidal tomography constrains earths deep-mantle
678 buoyancy. *Nature* **551** (7680), 321.
- 679 LAY, THORNE, HERNLUND, JOHN & BUFFETT, BRUCE A 2008 Core–mantle boundary heat flow.
680 *Nature geoscience* **1** (1), 25–32.
- 681 LIVERMORE, PHILIP W, BAILEY, LEWIS M & HOLLERBACH, RAINER 2016 A comparison of no-
682 slip, stress-free and inviscid models of rapidly rotating fluid in a spherical shell. *Scientific*
683 *reports* **6**, 22812.
- 684 MATSUI, HIROAKI, HEIEN, ERIC, AUBERT, JULIEN, AURNOU, JONATHAN M, AVERY,
685 MARGARET, BROWN, BEN, BUFFETT, BRUCE A, BUSSE, FRIEDRICH, CHRISTENSEN,
686 ULRICH R, DAVIES, CHRISTOPHER J & OTHERS 2016 Performance benchmarks for a
687 next generation numerical dynamo model. *Geochemistry, Geophysics, Geosystems* **17** (5),
688 1586–1607.
- 689 METMAN, MC, LIVERMORE, PW & MOUND, JE 2018 The reversed and normal flux
690 contributions to axial dipole decay for 1880–2015. *Physics of the Earth and Planetary*
691 *Interiors* **276**, 106–117.
- 692 MOUND, JON E & DAVIES, CHRISTOPHER J 2017 Heat transfer in rapidly rotating convection
693 with heterogeneous thermal boundary conditions. *Journal of Fluid Mechanics* **828**, 601–
694 629.
- 695 NAKAGAWA, TAKASHI 2011 Effect of a stably stratified layer near the outer boundary in
696 numerical simulations of a magnetohydrodynamic dynamo in a rotating spherical shell
697 and its implications for Earth’s core. *Physics of the Earth and Planetary Interiors* **187** (3),
698 342–352.
- 699 NAKAGAWA, TAKASHI 2015 An implication for the origin of stratification below the core–mantle
700 boundary region in numerical dynamo simulations in a rotating spherical shell. *Physics*
701 *of the Earth and Planetary Interiors* **247**, 94–104.
- 702 NAKAGAWA, T. & TACKLEY, P.J. 2008 Lateral variations in CMB heat flux and deep mantle
703 seismic velocity caused by a thermal–chemical-phase boundary layer in 3D spherical
704 convection. *Earth Planet. Sci. Lett.* **271** (1-4), 348–358.
- 705 NAKAGAWA, TAKASHI & TACKLEY, PAUL J 2013 Implications of high core thermal conductivity

- 706 on Earth's coupled mantle and core evolution. *Geophysical Research Letters* **40** (11),
707 2652–2656.
- 708 NIMMO, F. 2015 Thermal and compositional evolution of the core. In *Treatise on Geophysics*
709 *2nd Edn, Vol. 9* (ed. G. Schubert), pp. 209–219. Elsevier, Amsterdam.
- 710 OLSON, PETER 2009 Core dynamics. In *Treatise on Geophysics 1st Edn, Vol. 8* (ed. G. Schubert).
711 Elsevier, Amsterdam.
- 712 OLSON, PETER & CHRISTENSEN, UR 2002 The time-averaged magnetic field in numerical
713 dynamos with non-uniform boundary heat flow. *Geophysical Journal International*
714 **151** (3), 809–823.
- 715 OLSON, P., DEGUEN, R., RUDOLPH, M.L. & ZHONG, S. 2015 Core evolution driven by mantle
716 global circulation. *Phys. Earth Planet. Int.* **243**, 44–55.
- 717 OLSON, PETER, LANDEAU, MAYLIS & REYNOLDS, EVAN 2017 Dynamo tests for stratification
718 below the core-mantle boundary. *Physics of the Earth and Planetary Interiors* **271**, 1–18.
- 719 OTERO, JESSE, WITTENBERG, RALF W, WORTHING, RODNEY A & DOERING, CHARLES R
720 2002 Bounds on rayleigh–bénard convection with an imposed heat flux. *Journal of Fluid*
721 *Mechanics* **473**, 191–199.
- 722 PAPARELLA, F & YOUNG, W.R. 2002 Horizontal convection is non-turbulent. *J. Fluid Mech.*
723 **466**, 205–214.
- 724 POZZO, M., DAVIES, C., GUBBINS, D. & ALFÈ, D. 2012 Thermal and electrical conductivity of
725 iron at Earth's core conditions. *Nature* **485**, 355–358.
- 726 POZZO, MONICA, DAVIES, CHRIS, GUBBINS, DAVID & ALFÈ, DARIO 2013 Transport properties
727 for liquid silicon-oxygen-iron mixtures at Earth's core conditions. *Physical Review B*
728 **87** (1), 014110.
- 729 RÜCKRIEMEN, T., BREUER, D. & SPOHN, T. 2015 The Fe snow regime in Ganymede's core: A
730 deep-seated dynamo below a stable snow zone. *Journal of Geophysical Research: Planets*
731 **120** (6), 1095–1118, 2014JE004781.
- 732 SAHOO, S. & SREENIVASAN, B. 2017 On the effect of laterally varying boundary heat flux on
733 rapidly rotating spherical shell convection. *Physics of Fluids* **29** (8), 086602.

- 734 SCHAEFFER, N., JAULT, D., NATAF, H.-C. & FOURNIER, A. 2017 Turbulent geodynamo
735 simulations: a leap towards Earth's core. *Geophys. J. Int.* **211** (1), 1–29.
- 736 SCHUBERT, G & SODERLUND, KM 2011 Planetary magnetic fields: Observations and models.
737 *Physics of the Earth and Planetary Interiors* **187** (3-4), 92–108.
- 738 SHEARD, G.J., HUSSAM, W.K. & TSAI, T. 2016 Linear stability and energetics of rotating
739 radial horizontal convection. *J. Fluid Mech.* **795**, 1–35.
- 740 SHISHKINA, O. 2017 Mean flow structure in horizontal convection. *J. Fluid Mech.* **812**, 525–540.
- 741 SHISHKINA, OLGA, GROSSMANN, SIEGFRIED & LOHSE, DETLEF 2016 Heat and momentum
742 transport scalings in horizontal convection. *Geophys. Res. Lett.* **43** (3), 1219–1225.
- 743 SIGGERS, J.H., KERSWELL, R.R. & BALMFORTH, N.J. 2004 Bounds on horizontal convection.
744 *J. Fluid Mech.* **517**, 55–70.
- 745 SREENIVASAN, BINOD 2009 On dynamo action produced by boundary thermal coupling. *Physics
746 of the Earth and Planetary Interiors* **177** (3), 130–138.
- 747 SREENIVASAN, BINOD & GUBBINS, DAVID 2008 Dynamos with weakly convecting outer layers:
748 implications for core-mantle boundary interaction. *Geophysical and Astrophysical Fluid
749 Dynamics* **102** (4), 395–407.
- 750 SREENIVASAN, BINOD & GUBBINS, DAVID 2011 On mantle-induced heat flow variations at the
751 inner core boundary. *Phys. Earth Planet. Int.* **187** (3), 336–341.
- 752 STANLEY, S. & GLATZMAIER, G.A. 2010 Dynamo models for planets other than earth. *Space
753 Sci Rev* **152**, 617–649.
- 754 STANLEY, SABINE & MOHAMMADI, AYLIA 2008 Effects of an outer thin stably stratified layer
755 on planetary dynamos. *Physics of the Earth and Planetary Interiors* **168** (3), 179–190.
- 756 STEVENSON, DAVID J 2001 Mars' core and magnetism. *Nature* **412** (6843), 214.
- 757 TAKAHASHI, FUTOSHI, TSUNAKAWA, HIDEO, MATSUSHIMA, MASAKI, MOCHIZUKI, NOBUTATSU
758 & HONKURA, YOSHIMORI 2008 Effects of thermally heterogeneous structure in the
759 lowermost mantle on the geomagnetic field strength. *Earth and Planetary Science Letters*
760 **272** (3), 738–746.
- 761 TAKEHIRO, SHIN-ICHI & LISTER, JOHN R 2001 Penetration of columnar convection into an

- 762 outer stably stratified layer in rapidly rotating spherical fluid shells. *Earth and Planetary*
763 *Science Letters* **187** (3), 357–366.
- 764 WILLIAMS, JEAN-PIERRE & NIMMO, FRANCIS 2004 Thermal evolution of the Martian core:
765 Implications for an early dynamo. *Geology* **32** (2), 97–100.
- 766 WILLIS, ASHLEY P, SREENIVASAN, BINOD & GUBBINS, DAVID 2007 Thermal core-mantle
767 interaction: exploring regimes for ‘locked’ dynamo action. *Phys. Earth Planet. Int.* **165** (1),
768 83–92.
- 769 ZHANG, KEKE & GUBBINS, DAVID 1992 On convection in the Earth’s core driven by lateral
770 temperature variations in the lower mantle. *Geophys. J. Int.* **108** (1), 247–255.
- 771 ZHANG, KEKE & GUBBINS, DAVID 1993 Convection in a rotating spherical fluid shell with
772 an inhomogeneous temperature boundary condition at infinite Prandtl number. *J. Fluid*
773 *Mech.* **250**, 209–232.

774 Appendix A. Summary tables

775 Summary tables of the model resolution, control parameters and selected output
776 parameters for all simulations. In all cases $Pr = 1$ and the shell aspect ratio $\eta = 0.35$
777 for models in tables A.1 to A.3 and $\eta = 0.01$ for models in table A.4. Definitions for
778 B , S and $Ra_{\mathcal{H}}$ are given in 2.1. The quantity $N/2\Omega$, defined in (5.6), is the ratio of the
779 Brunt-Väisälä frequency, N , to the rotation rate Ω . The variable n_r is the number of
780 radial points within the fluid shell, l_{max} is the maximum degree of the spherical harmonic
781 expansion ($=m_{max}$, the maximum order of the expansion). Since $Re = Pe = \langle u^* \rangle_v$, the
782 Rossby number is

$$Ro = 2 Re E = 2 \langle u^* \rangle_v E. \quad (\text{A1})$$

B	S	$Ra_{\mathcal{H}}$	n_r	l_{max}	$\frac{N}{2\Omega}$	Re	Ro	State
0.01	0.001	10^2	32	32	3.16×10^{-5}	0.03	6.30×10^{-6}	steady
0.1	0.001	10^3	32	32	1.00×10^{-4}	0.08	1.58×10^{-5}	steady

1	0.001	10^4	48	48	3.16×10^{-4}	0.72	1.44×10^{-4}	steady
1	0.01	10^4	60	48	1.00×10^{-3}	0.72	1.44×10^{-4}	steady
1	0.1	10^4	60	48	3.16×10^{-3}	0.72	1.43×10^{-4}	steady
1	1	10^4	60	48	1.00×10^{-2}	0.69	1.38×10^{-4}	steady
1	10	10^4	60	48	3.16×10^{-2}	0.41	8.14×10^{-5}	steady
1	100	10^4	60	48	1.00×10^{-1}	0.08	1.68×10^{-5}	steady
1	1000	10^4	60	48	3.16×10^{-1}	0.02	3.23×10^{-6}	steady
1	10000	10^4	60	48	1.00	0.003	5.69×10^{-7}	steady
5	0.001	5×10^4	48	48	7.10×10^{-4}	3.11	6.22×10^{-4}	steady
5	0.01	5×10^4	48	48	2.24×10^{-3}	3.11	6.22×10^{-4}	steady
5	0.1	5×10^4	48	48	7.10×10^{-3}	3.06	6.13×10^{-4}	steady
5	1	5×10^4	48	48	2.24×10^{-2}	2.49	4.98×10^{-4}	steady
10	0.001	10^5	60	48	1.00×10^{-3}	5.22	1.04×10^{-3}	steady
10	0.01	10^5	48	48	3.16×10^{-3}	5.22	1.04×10^{-3}	steady
10	0.1	10^5	48	48	1.00×10^{-2}	5.01	1.01×10^{-3}	steady
10	1	10^5	60	48	3.16×10^{-2}	3.55	7.10×10^{-4}	steady
10	10	10^5	60	48	1.00×10^{-1}	0.84	1.69×10^{-4}	steady
10	100	10^5	60	48	3.16×10^{-1}	0.16	3.24×10^{-5}	steady
10	1000	10^5	60	48	1.00	0.03	5.70×10^{-6}	steady
10	10000	10^5	80	64	3.16	0.005	9.58×10^{-7}	steady
100	0.001	10^6	96	96	3.16×10^{-3}	17.45	3.49×10^{-3}	steady
100	0.01	10^6	96	96	1.00×10^{-2}	17.25	3.45×10^{-3}	steady
100	0.1	10^6	80	64	3.16×10^{-2}	15.21	3.04×10^{-3}	steady
100	1	10^6	80	64	1.00×10^{-1}	8.50	1.70×10^{-3}	steady
100	10	10^6	80	64	3.16×10^{-1}	1.66	3.33×10^{-4}	steady

100	100	10^6	80	64	1.00	0.29	5.76×10^{-5}	steady
100	10000	10^6	224	224	10.0	0.008	1.60×10^{-6}	steady
1000	0.001	10^7	256	256				unsteady
1000	0.01	10^7	96	96				unsteady
1000	0.1	10^7	160	160				periodic
1000	1	10^7	96	96	3.16×10^{-1}	27.99	5.60×10^{-3}	steady
1000	10	10^7	96	96	1.00	2.86	5.72×10^{-4}	steady
1000	100	10^7	64	64	3.16	0.48	9.59×10^{-5}	steady
1000	1000	10^7	192	192	10.0	0.08	1.60×10^{-5}	steady
1000	10000	10^7	224	224	31.6	0.01	2.70×10^{-6}	steady
10000	1	10^8	64	64	1.00	39.73	7.95×10^{-3}	steady
10000	10	10^8	64	64	3.16	4.79	9.58×10^{-4}	steady
10000	100	10^8	128	128	10.0	0.80	1.60×10^{-4}	steady
10000	1000	10^8	64	64	31.6	0.14	2.70×10^{-5}	steady
100000	1	10^9	64	64	3.16	52.57	1.05×10^{-2}	steady
1000000	1	10^{10}	96	96	10.0	97.37	1.95×10^{-2}	steady

Table A.1: Summary of all numerical simulations with $E = 10^{-4}$.

B	S	$Ra_{\mathcal{H}}$	n_r	l_{max}	$\frac{N}{2\Omega}$	Re	Ro	State
1	0.001	10^5	48	48	1.00×10^{-4}	0.75	1.49×10^{-5}	steady
1	0.01	10^5	48	48	3.16×10^{-4}	0.75	1.49×10^{-5}	steady
1	0.1	10^5	48	48	1.00×10^{-3}	0.75	1.49×10^{-5}	steady
1	1	10^5	48	48	3.16×10^{-3}	0.73	1.46×10^{-5}	steady
1	10	10^5	64	64	1.00×10^{-2}	0.45	9.02×10^{-6}	steady
1	100	10^5	64	64	3.16×10^{-2}	0.10	2.07×10^{-6}	steady

1	1000	10^5	64	64	0.1	0.02	4.51×10^{-7}	steady
10	0.001	10^6	48	48	3.16×10^{-4}	5.49	1.10×10^{-4}	steady
10	1	10^6	48	48	1.00×10^{-2}	3.96	7.92×10^{-5}	steady
10	10	10^6	64	64	3.16×10^{-2}	1.04	2.07×10^{-5}	steady
10	100	10^6	64	64	1.00×10^{-1}	0.23	4.51×10^{-6}	steady
10	1000	10^6	64	64	3.16×10^{-1}	0.05	9.12×10^{-7}	steady
100	0.001	10^7	48	48	1.00×10^{-3}	20.74	4.15×10^{-4}	steady
100	0.01	10^7	96	96	3.16×10^{-3}	20.57	4.11×10^{-4}	steady
100	0.1	10^7	96	96	1.00×10^{-2}	18.43	3.69×10^{-4}	steady
100	1	10^7	48	48	3.16×10^{-2}	10.20	2.04×10^{-4}	steady
100	10	10^7	96	96	1.00×10^{-1}	2.37	4.75×10^{-5}	steady
100	100	10^7	96	96	3.16×10^{-1}	0.47	9.35×10^{-6}	steady
100	10000	10^7	192	192	3.16	0.02	3.10×10^{-7}	steady
1000	0.01	10^8	160	160				unsteady
1000	0.1	10^8	128	128				unsteady
1000	1	10^8	128	128	1.00×10^{-1}	43.64	8.73×10^{-4}	steady
1000	10	10^8	128	128	3.16×10^{-1}	6.00	1.20×10^{-4}	steady
1000	100	10^8	128	128	1.00	0.87	1.75×10^{-5}	steady
10000	0.01	10^9	128	128				unsteady
10000	0.1	10^9	128	128				unsteady
10000	1	10^9	128	128	3.16×10^{-1}	218.25	4.36×10^{-3}	steady
10000	10	10^9	128	128	10.0	10.36	2.07×10^{-4}	steady
10000	100	10^9	128	128	3.16	1.55	3.10×10^{-5}	steady
100000	1	10^{10}	64	64	1.00	420.48	8.41×10^{-3}	steady

Table A.2: Summary of all numerical simulations with $E = 10^{-5}$.

B	S	$Ra_{\mathcal{H}}$	n_r	l_{max}	$\frac{N}{2\Omega}$	Re	Ro	State
10	0.001	10^7	96	96	1.00×10^{-4}	5.57	1.11×10^{-5}	steady
10	0.01	10^7	96	96	3.16×10^{-4}	5.56	1.11×10^{-5}	steady
10	0.1	10^7	96	96	1.00×10^{-3}	5.54	1.11×10^{-5}	steady
10	1	10^7	96	96	3.16×10^{-3}	4.17	8.34×10^{-6}	steady
10	10	10^7	96	96	1.00×10^{-2}	1.13	2.25×10^{-6}	steady
10	100	10^7	192	192	3.16×10^{-2}	0.27	5.33×10^{-7}	steady
100	0.001	10^8	128	128	3.16×10^{-4}	22.69	4.54×10^{-5}	steady
100	0.01	10^8	128	128	1.00×10^{-3}	22.37	4.47×10^{-5}	steady
100	0.1	10^8	128	128	3.16×10^{-3}	20.04	4.01×10^{-5}	steady
100	1	10^8	96	96	1.00×10^{-2}	11.43	2.29×10^{-5}	steady
100	10	10^8	96	96	3.16×10^{-2}	2.81	5.26×10^{-7}	steady
1000	0.1	10^9	160	160				unsteady
1000	10	10^9	96	96	1.00×10^{-1}	9.91	1.98×10^{-5}	steady
1000	100	10^9	224	224	3.16×10^{-1}	1.34	2.68×10^{-6}	steady

 Table A.3: Summary of all numerical simulations with $E = 10^{-6}$.

E	B	S	$Ra_{\mathcal{H}}$	n_r	l_{max}	$\frac{N}{2\Omega}$	Re	Ro
10^{-4}	1	0.001	10000	48	48	3.16×10^{-4}	0.300872	0.601744×10^{-4}
10^{-4}	1	1	10000	48	48	1.00×10^{-2}	0.295070	0.590139×10^{-4}
10^{-4}	1	10	10000	48	48	3.16×10^{-2}	0.217627	0.435254×10^{-4}
10^{-4}	1	100	10000	48	48	1.00×10^{-1}	0.064906	0.129813×10^{-4}

10^{-4}	1	1000	10000	48	48	3.16×10^{-1}	0.013037	0.260743×10^{-5}
10^{-4}	10	1	10000	48	48	3.16×10^{-2}	2.243120	0.448624×10^{-3}
10^{-4}	10	10	10000	48	48	1.00×10^{-2}	1.056216	0.211243×10^{-3}
10^{-4}	10	100	10000	48	48	3.16×10^{-1}	0.594569	0.118914×10^{-3}
10^{-4}	100	1	10000	48	48	1.00×10^{-1}	11.922864	0.238457×10^{-2}
10^{-4}	100	10	10000	48	48	3.16×10^{-1}	11.787036	0.235741×10^{-2}
10^{-4}	100	100	10000	48	48	1.00	0.243352	0.486704×10^{-4}
10^{-4}	100	1000	10000	48	48	3.16	0.041440	0.828798×10^{-5}

Table A.4: Summary of all numerical simulations with $E = 10^{-4}$ and shell aspect ratio $\eta = 0.01$.

783 **Appendix B. Scaling analysis figures**

784 Example figures of the term balances in the vorticity and temperature equations for
785 a few representative high and low S models. These figures are used to verify our scaling
786 predictions (i.e. that we have used the correct length scales in various terms) and to
787 justify only considering certain terms in the governing equation in the scaling analyses,
788 as they make clear that the balances we consider are both applicable in our two S regimes,
789 appropriately scaled in our analysis and that our volume-averaged model diagnostics are
790 appropriate (as we could have chosen other diagnostic outputs from the simulations).

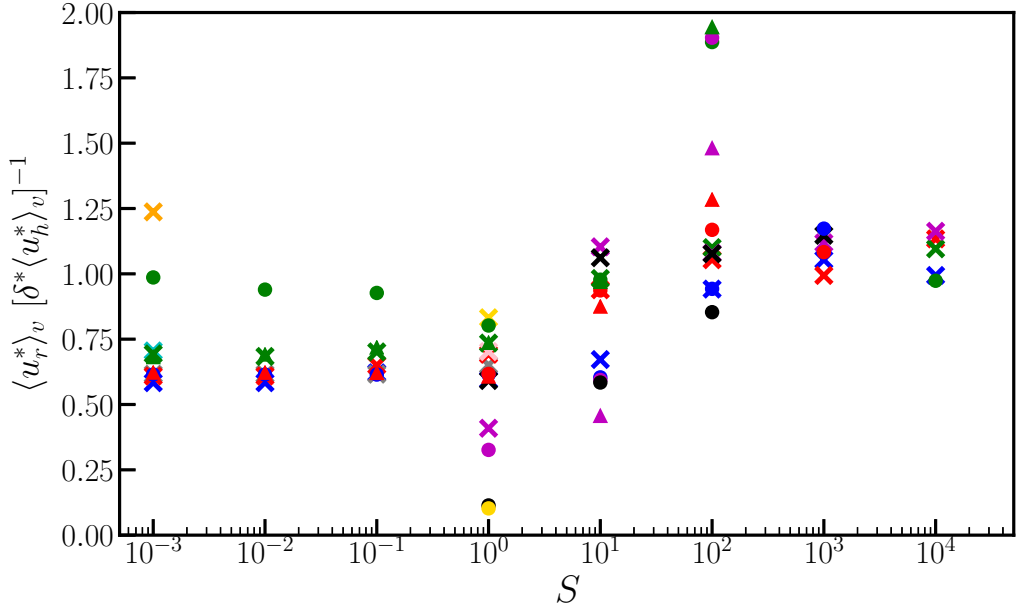
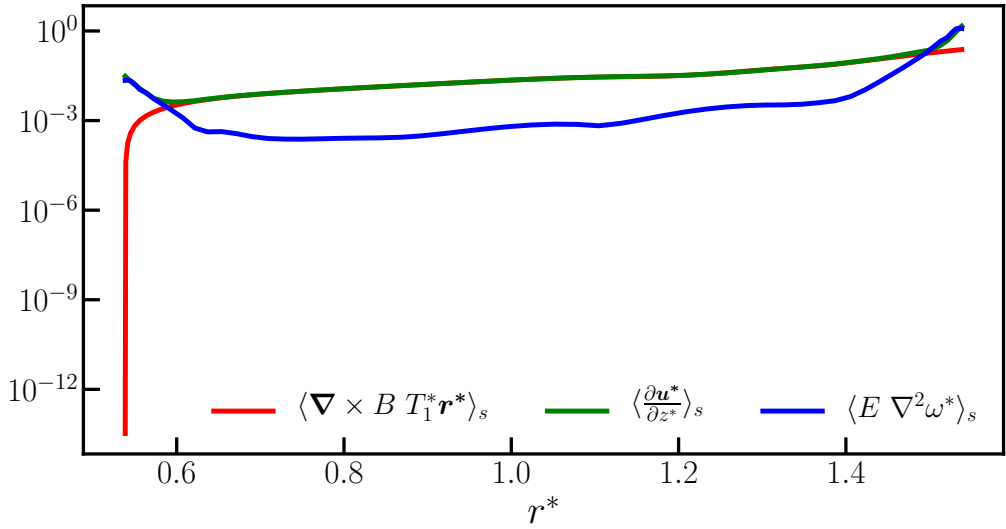


Figure B.1: Radial velocity scaled by $\delta^* \langle u_h^* \rangle_v$, where $\langle u_h^* \rangle_v$ is the average volume-averaged horizontal velocity, as a function of the stratification parameter, S , for all steady models. Symbol shapes represent the Ekman number, E , and colours represent the buoyancy parameter, B . The key is given in fig 6a.



(b) $B = 1000, S = 1000$

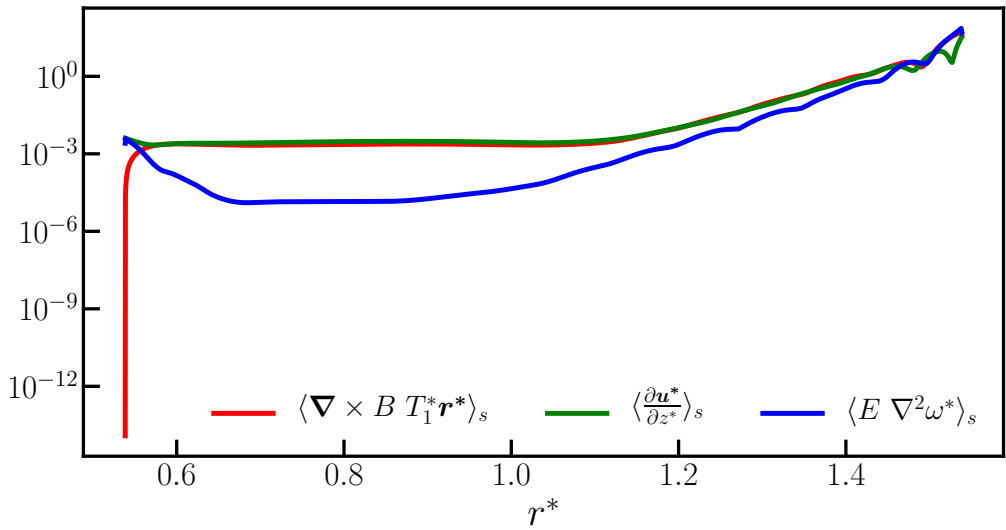


Figure B.2: All terms (denoted by line colour) in the dimensionless vorticity equation as a function of radius for two representative $E = 10^{-4}$ models at high stratification parameter ($S = 1000$) and (a) $B = 1$ and (b) $B = 1000$.

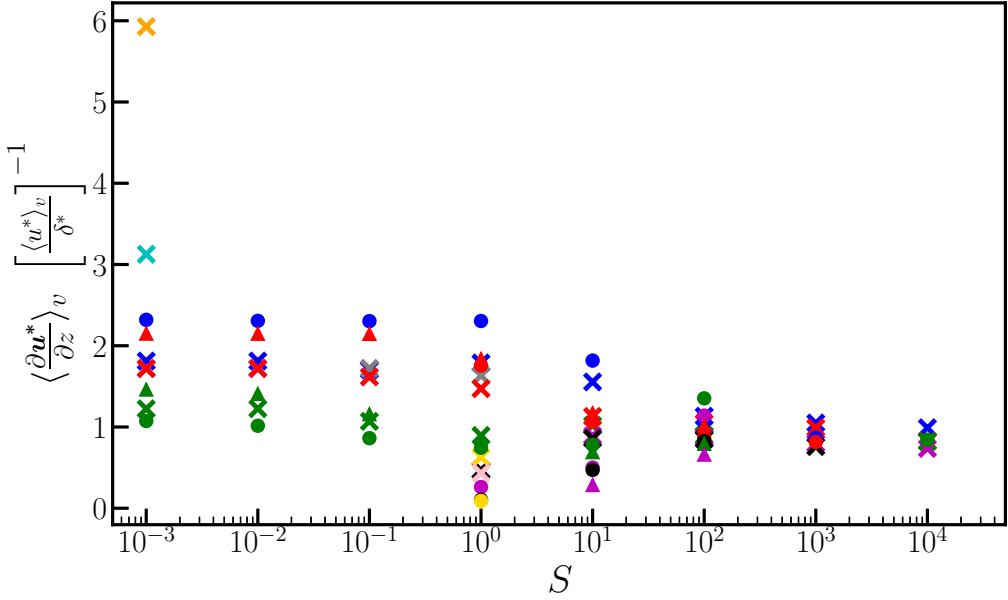


Figure B.3: Volume-averaged Coriolis term of the vorticity equation ($\frac{\partial \mathbf{u}^*}{\partial z}$), scaled by our approximation to that term ($\langle u^* \rangle_v / \delta^*$), as a function of the stratification parameter, S , for all steady models. Symbol shapes represent the Ekman number, E , and colours represent the buoyancy parameter, B . The key is given in fig 6a.

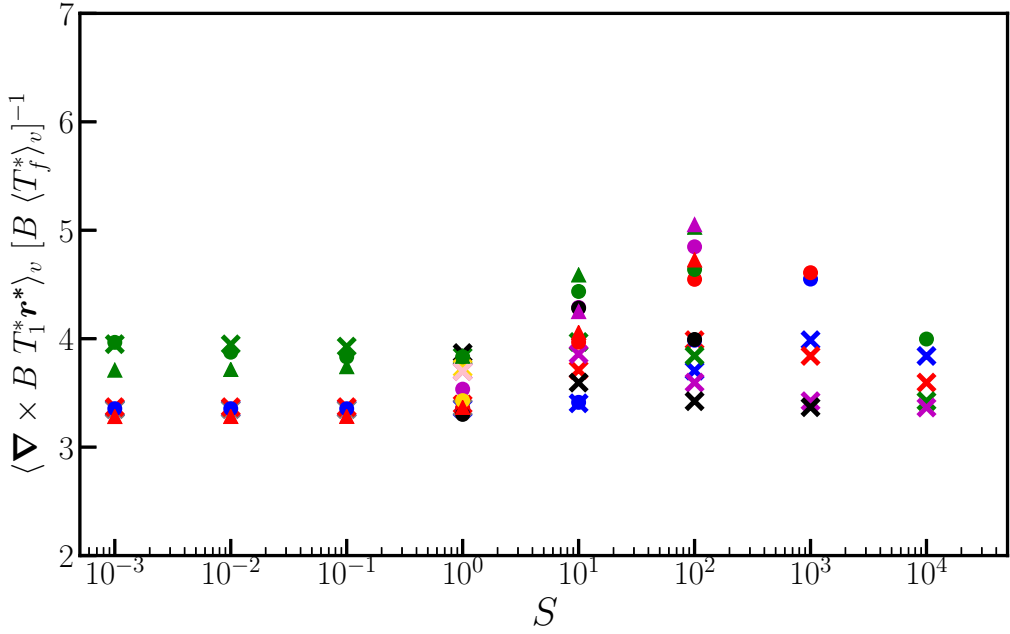


Figure B.4: Volume-averaged buoyancy term of the vorticity equation ($\nabla \times B T_1^* \mathbf{r}^*$), scaled by our approximation to that term ($B \langle T_f^* \rangle_v$), as a function of the stratification parameter, S , for all steady models. Symbol shapes represent the Ekman number, E , and colours represent the buoyancy parameter, B . The key is given in fig 6a.

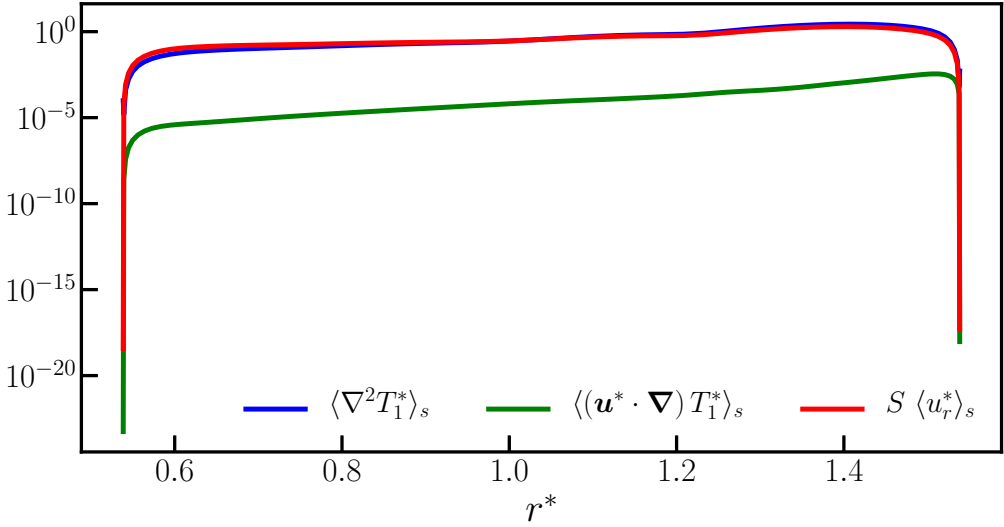
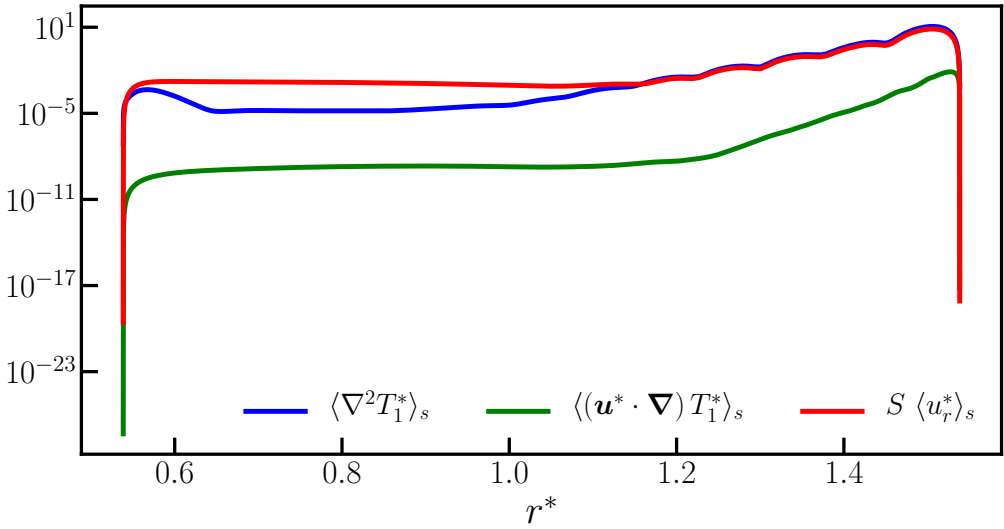
(a) $B = 1, S = 1000$

 (b) $B = 1000, S = 1000$


Figure B.5: All terms (denoted by line colour) in the dimensionless temperature equation as a function of radius for two representative $E = 10^{-4}$ models at high stratification parameter ($S = 1000$) and (a) $B = 1$ and (b) $B = 1000$.

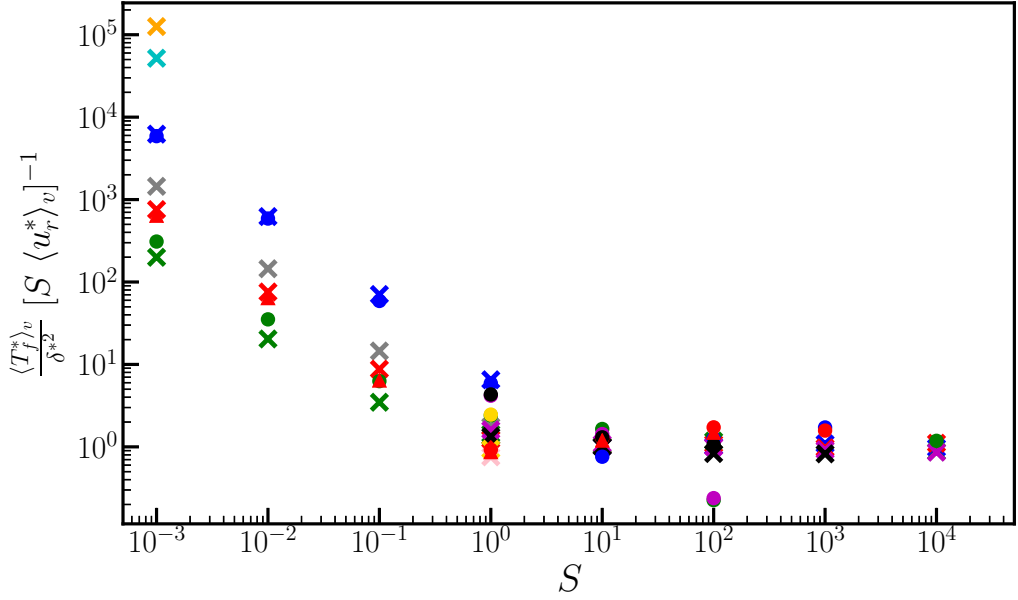


Figure B.6: Ratio of the two dominant terms in the temperature equation as a function of the stratification parameter, S , for all steady models. Symbol shapes represent the Ekman number, E , and colours represent the buoyancy parameter, B . The key is given in fig 6a.

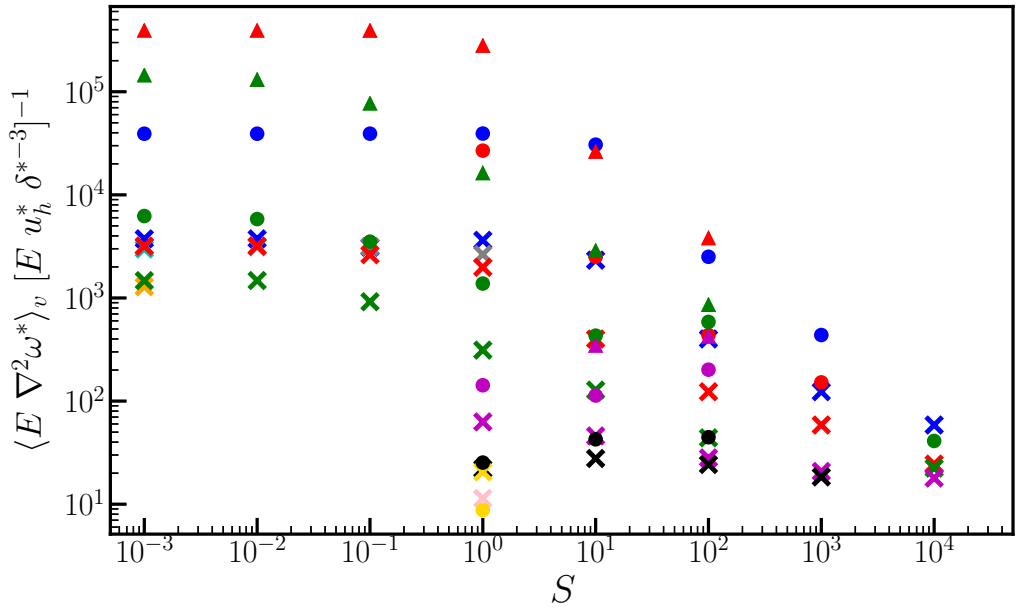
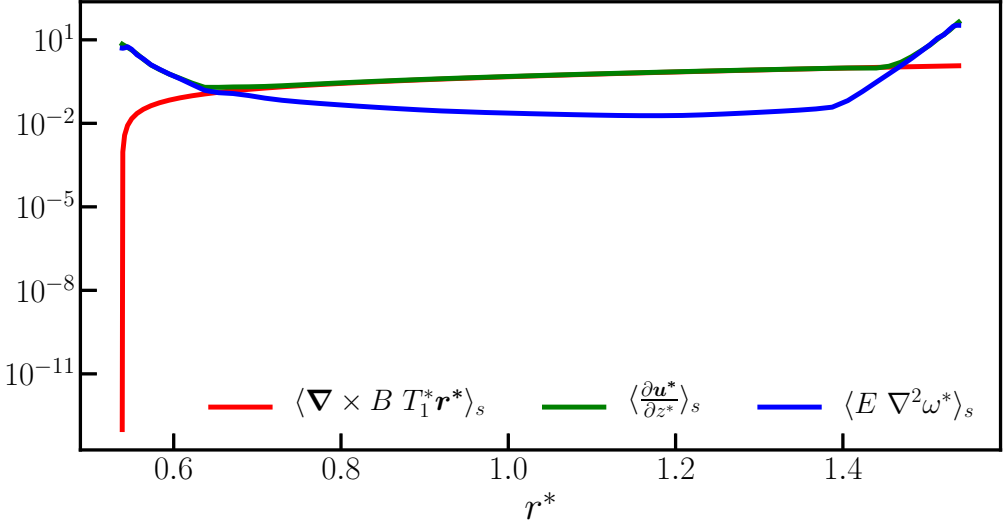


Figure B.7: Volume-averaged viscous term of the vorticity equation ($E \nabla^2 \omega^*$), scaled by the (incorrect) approximation to that term ($E u_h^* \delta^{*-3}$), as a function of the stratification parameter, S , for all steady models. Symbol shapes represent the Ekman number, E , and colours represent the buoyancy parameter, B . The key is given in fig 6a.

(a) $B = 1, S = 0.01$



(b) $B = 100, S = 0.01$

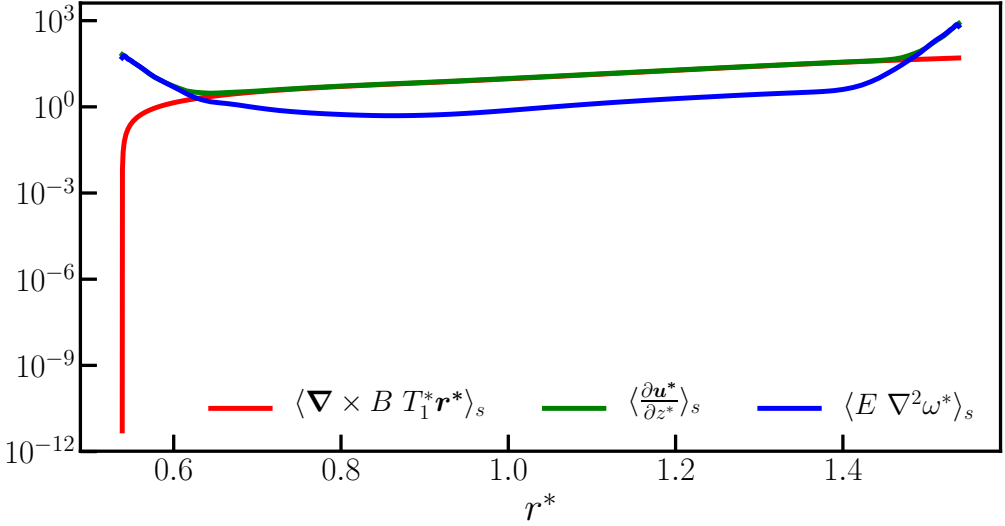
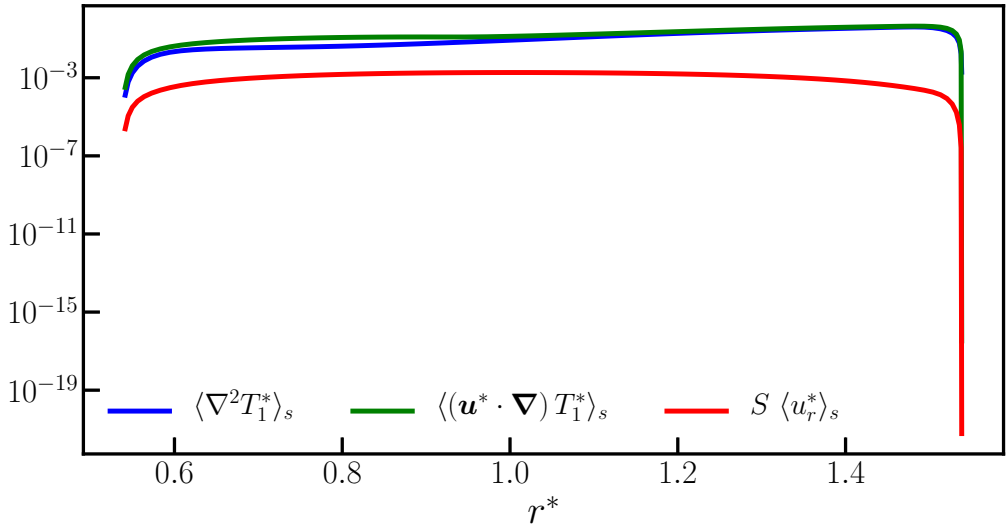


Figure B.8: All terms (denoted by line colour) in the dimensionless vorticity equation as a function of radius for two representative $E = 10^{-4}$ models at low stratification parameter ($S = 0.01$) and (a) $B = 1$ and (b) $B = 100$.



(b) $B = 100, S = 0.01$

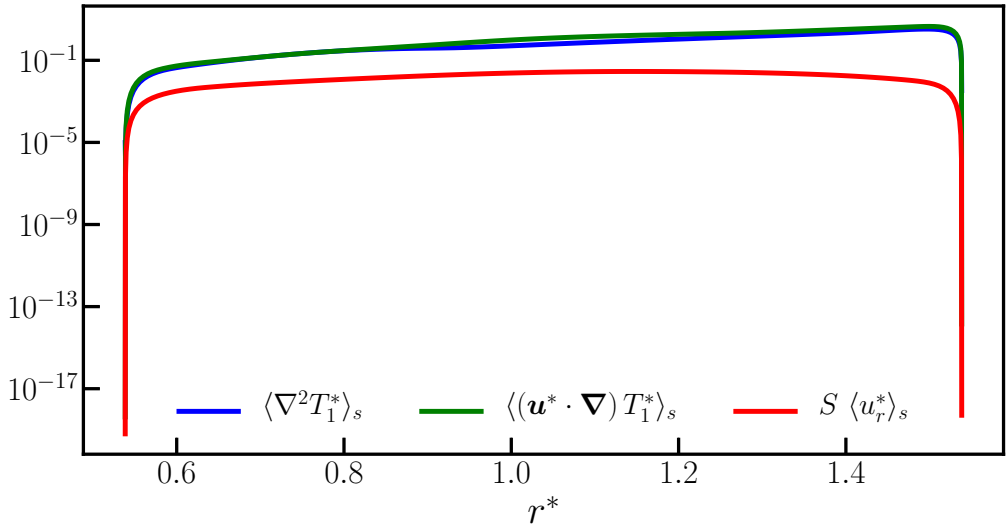
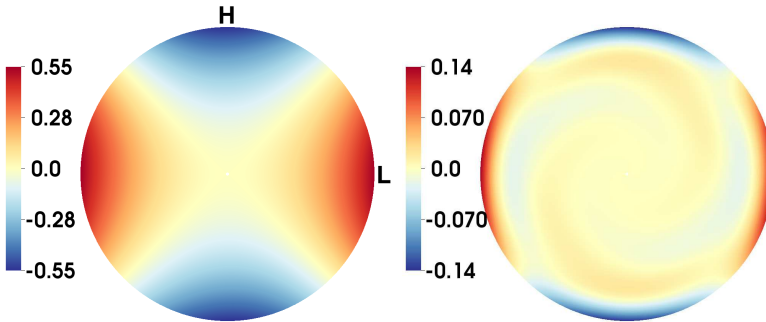


Figure B.9: All terms (denoted by line colour) in the dimensionless temperature equation as a function of radius for two representative $E = 10^{-4}$ models at low stratification parameter ($S = 0.01$) and (a) $B = 1$ and (b) $B = 100$.

791 **Appendix C. Low shell aspect ratio dynamics**

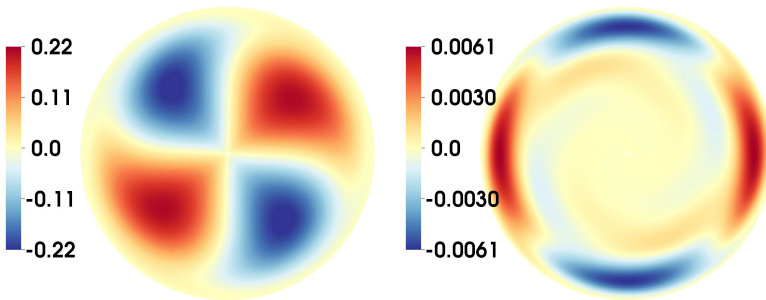
a: $S = 0.001, T_f^*$

b: $S = 1000, T_f^*$



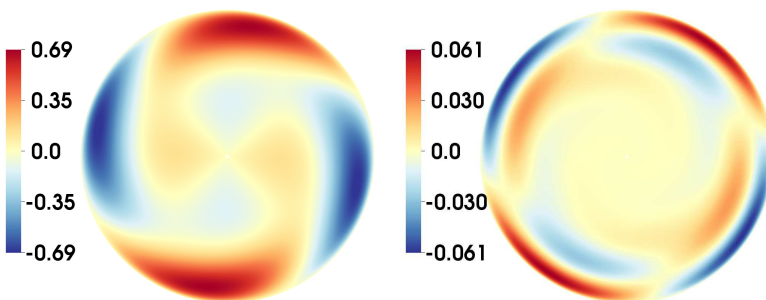
c: $S = 0.001, u_r^*$

d: $S = 1000, u_r^*$



e: $S = 0.001, u_\phi^*$

f: $S = 1000, u_\phi^*$



792 Figure C.1: Equatorial plots of T_f^* (top), u_r^* (middle) and u_ϕ^* (bottom) for models with shell aspect ratio $\eta = 0.01$ at $E = 10^{-4}$, $B = 1$ and $S = 0.001$ (left) and 1000 (right). Red indicates positive values and blue indicates negative values. Note the different colour scales. Locations of high (H) and low (L) outward heat flux are shown on the top left.